American Mineralogist, Volume 91, pages 1385–1400, 2006

Effect of melt structure on trace-element partitioning between clinopyroxene and silicic, alkaline, aluminous melts

F. HUANG,[1,*] C.C. LUNDSTROM,[1] AND W.F. MCDONOUGH[2]

[1]Department of Geology, University of Illinois at Urbana-Champaign, 1301 W. Green St., Illinois 61801, U.S.A.
[2]Department of Geology, University of Maryland, College Park, Maryland 20742, U.S.A.

ABSTRACT

We have investigated trace-element partitioning between clinopyroxene and silicic melts ranging from 62 to 69 wt% SiO_2 in piston-cylinder experiments at 1.1 GPa and 1145–1155 °C. Run products consist of diopsidic clinopyroxene (with 3–5 wt% Al_2O_3 and ~1 wt% Na_2O) coexisting with silicic, aluminous, and alkaline melts. Clinopyroxene-melt partition coefficients for rare earth elements (REE) are significantly higher (e.g., $D_{Sm} = 0.76$ to 3.1) than previous studies of clinopyroxene-basaltic melt partitioning. The maximum D_{REE} is also shifted toward middle REE (e.g., Tb). Although the partition coefficients of Sr and Ti ($D_{Sr} = 0.23$–0.39, $D_{Ti} = 0.28$–1.0) are also elevated relative to clinopyroxene-basaltic melt, partition coefficients for Zr and Li (0.14–0.23 and 0.16–0.25, respectively) are within the range of literature values.

The high partition coefficients for REE, Sr, and Ti in this study do not reflect crystal-compositional effects. For instance, no relationship is observed between ^{IV}Al and these partition coefficients. REE and Ti partition coefficients correlate poorly with jadeite component of the clinopyroxene; however, the elevated Na_2O contents of both the melt and clinopyroxene make it difficult to discriminate fully the effect of jadeite component from the effect of changes in melt structure. The non-bridging oxygen to tetrahedral cation ratio (NBO/T; Mysen et al. 1985) varies from 0.08 to 0.17 and roughly correlates with $^{cpx/melt}D_{REE}$, consistent with a recent study (Gaetani 2004) that concluded that melt structure significantly affects partitioning when NBO/T < 0.49. Notably, we find a strong correlation between the molar $Ca^{2+}/(M^{+} + M^{2+})$ of the melt and the optimum D (D_0) for the REE, indicating that melt structure, and not jadeite content, is the dominant control on clinopyroxene-melt partitioning in these experiments.

The partition coefficients for the REE, Ti, Zr, and Sr are in good agreement with observed clinopyroxene-silicic glass partitioning within mantle xenoliths (Chazot et al. 1996; Vannucci et al. 1998), indicating these results may apply to lithospheric melting. Furthermore, the origin of hump-shaped REE patterns observed in residual clinopyroxene from abyssal peridotites could be explained if shallow depleted melts of peridotite are silica-rich. A two-stage fractional melting model assuming clinopyroxene-silicic melt partitioning at shallow mantle depths from 10 to 30 km beneath a mid-ocean ridge can reproduce the observed hump-shaped REE patterns. If so, hump-shaped REE patterns may provide evidence for the existence and extraction of silica-rich melt created in the shallow mantle.

Keywords: Melt structure, partition coefficient, trace element, clinopyroxene

INTRODUCTION

There is increasing awareness of the range in melt compositions created during mantle melting and a corresponding acceptance that erupted magmas reflect integration and mixing of these diverse melts. Although their role in ultimately contributing to erupted lavas is unclear, glasses enriched in silica, alumina, and alkalis are often observed in mantle xenoliths, with several studies suggesting these melts may contribute to aggregate ocean island basalts (Wulff-Pedersen et al. 1996, 1999; Vannucci et al. 1998; Lundstrom et al. 2003). Consistent with this, phase-equilibria experiments show that some silica-rich glasses observed in xenoliths are in equilibrium with harzburgitic and lherzolitic mineral assemblages at 1.0–1.5 GPa and ~1150 °C (Draper and Green 1997, 1999), indicating that they represent a plausible melt component contributing to mantle-derived magmas.

Clinopyroxene (cpx) is generally considered the most important mineral controlling the partitioning of trace elements between melt and residual solid during mantle melting (e.g., McKenzie and O'Nions 1991). The partitioning of trace elements between silicate melts and minerals depends on both crystal chemistry and melt structure. Several recent studies have demonstrated the importance of crystal-chemical control on trace-element partitioning between cpx and basaltic melt, with a particular emphasis on the site size energetics of an element substitution (e.g., Blundy and Wood 1994). Notably, the effect

* E-mail: fhuang1@uiuc.edu

of melt structure and polymerization on partitioning of trace elements has been much less discussed in the recent literature than the effect of crystal composition, despite the realization of its importance during early partitioning studies (Ryerson and Hess 1978; Mysen and Virgo 1980).

Partition coefficients between silicic, alkaline, aluminous melts, and coexisting mantle minerals are required to determine whether silicic melts could have significantly contributed to erupted magmas. Indeed, because mixing would likely obscure observation of such melt compositions, evidence of such melt may only be found in residual minerals that have undergone element partitioning in the presence of silicic melt. To understand the partitioning of trace elements between cpx and silica-rich melts, we have conducted piston-cylinder experiments using two different starting materials at 1.1 GPa and ~1150 °C. By comparing trace-element partitioning between cpx of relatively constant composition and melts of differing silica ± alkali contents, we can evaluate the effect of melt structure on mineral-melt partitioning of trace elements. We then apply our results to a model of fractional melting to attempt to explain observed hump-shaped rare earth element (REE) patterns in residual cpx from some abyssal peridotites (Johnson et al. 1990; Hellebrand et al. 2002; Hellebrand and Snow 2003).

Experimental methods

Starting materials

We investigated two different starting materials: a dacitic melt modeled after the experiments of Draper and Green (1999) and a more silicic melt based on an observed glass composition in a harzburgite xenolith from the Canary Islands (Vannucci et al. 1998) (Table 1). Composition MEDSIL (medium-silica) is a synthetic powder similar to DG-1 in Draper and Green (1999), which is multiply saturated in olivine, orthopyroxene, and cpx in the pressure range of 1.0–1.1 GPa and temperature range of 1125–1150 °C. Starting material HISIL (high-silica) is a synthetic powder, made to correspond to coexisting silica-rich glass (90% by mass) and chromian diopside (10%) in a harzburgite xenolith (PAT2-68; Vannucci et al. 1998). Note that the starting materials in this study were chosen not to constrain partitioning during melting of fertile mantle but rather element partitioning between depleted peridotite and silica-rich melt; such melts could be produced by the process of diffusive infiltration of alkali (DIA) occurring at pressures of 1.0 GPa or less (Lundstrom 2000; Lundstrom et al. 2003).

Starting materials were synthesized by mixing high purity oxides of Si, Al, Mg, Ti, and Cr, and carbonates of Na, K, and Ca. These materials were hand ground under ethanol for 2 h in an agate mortar. This powder was then doped with a variety of trace elements as nitrate solutions, resulting in ~0.5 wt% total trace elements. Cesium, Rb, and Ba contents are at the ~800 ppm level; Nb, Hf, Ta, Pb, Th, U, Sr, Zr, La, Nd, Sm, Eu, Er, and Yb contents are at the 75–300 ppm level; the starting material for MEDSIL5244, MEDSIL1035A, and MEDSIL1035B was additionally doped with 300 ppm Tb. Lithium was not doped intentionally, but was found at ~60 ppm in the starting material due to impurities in the reagents. The resulting powders were decarbonated by heating at 1000 °C for 4 h and then fused at 1450 °C for 4 h. The glass was ground to a powder, high-purity FeO was added to bring the mixture to the desired bulk composition, ground again under ethanol, and stored in an oven at 120 °C.

Based on our early experiments that produced only a few small crystals, we added ~9 wt% natural wollastonite ($CaSiO_3$) powder to the MEDSIL composition to increase the cpx mode and crystal size. Similarly, we added ~5 wt% diopside glass powder to the HISIL composition to increase the amount of cpx. Samples MEDSIL2161, MEDSIL2601, and MEDSIL9273 represent successful experiments using the MEDSIL composition, and samples MEDSIL5244, MEDSIL1035A, and MEDSIL1035B reflected the MEDSIL+9% $CaSiO_3$. Sample HISIL7262 was made using the HISIL composition, and HISIL9163 and HISIL5244 using HISIL + 5% diopside glass (Table 1).

Experimental techniques

Experiments were conducted in graphite capsules at 1.1 GPa in a piston-cylinder apparatus using 3/4" salt-Pyrex assemblies. Temperature was measured and controlled using either a $WRe_{5\%}$-$WRe_{25\%}$ or Pt-$PtRh_{10\%}$ thermocouple positioned 1 mm above the sample. We switched to using Pt-$PtRh_{10\%}$ in later experiments because of unacceptable thermocouple drifting in many early $WRe_{5\%}$-$WRe_{25\%}$ experiments (particularly those at lower pressures; see Pertermann and Lundstrom 2006).

Time-temperature paths for the experiments also evolved over the course of the study (Table 2, Fig. 1). The earliest experiments (MEDSIL2601 and MEDSIL2161) began by homogenizing the melt at 1445 °C for 5.5 h, ramping down to the final temperature (1150 °C) at 600 °C/h and quenching after dwelling at 1150 °C for ~18.5 h. For other experiments (HISIL7262, HISIL9163, MEDSIL9273), melts were homogenized at 1300 °C for 24 h, then held at 1200 °C for 2 h, stepped down to just below the liquidus (1185 °C) and then ramped to the final temperature at 0.5–1 °C/h (Fig. 1). Cpx produced by these cooling paths were often too small to be analyzed or contained some melt inclusions, largely reflecting nucleation problems associated with the silica-rich melt. To improve the size and quality of the crystals, we implemented a cycled time-temperature path for experiment MEDSIL5244 and HISIL5244. The temperature was maintained at 1300 °C for 6 min, dropped to 1200 °C for 5 h, stepped to the liquidus (1185 °C), and immediately ramped to 1165 °C at 1 °C/h. Once reaching 1165 °C, the temperature was increased rapidly back to 1200 °C, held for 5 h, stepped, and cooled as in the first cycle, but with a final temperature of 1155 °C.

Table 1. Major element composition (wt%) of starting materials

	MEDSIL Composition			HISIL composition		
Element	*DG*-1	MEDSIL	MEDSIL + 9% $CaSiO_3$	PAT2-68	HISIL	HISIL + 5% diopside
SiO_2	61.13	62.96	62.00	69.06	68.53	67.91
Al_2O_3	17.06	16.00	14.64	16.94	14.94	14.23
FeO	2.16	2.18	1.99	1.74	1.65	1.57
MgO	4.8	4.46	4.08	1.15	2.67	3.43
CaO	1.4	2.11	6.04	1.32	3.37	4.44
Na_2O	5.73	5.22	4.78	4.92	4.68	4.46
K_2O	7.36	6.63	6.07	4.64	3.97	3.78
TiO_2	0.37	0.42	0.38	0.08	0.14	0.13
Cr_2O_3	–	–	–	–	0.04	0.04
Total	100	100	100	99.91	100	100

Notes: *DG*-1 is from Draper and Green (1999). PAT2-68 is from the glass composition in harzburgite xenolith (PAT2-68) from Vannucci et al. (1998).

Table 2. Summary of conditions of experiments

Experiment	MEDSIL2601	MEDSIL9273	MEDSIL5244 and HISIL5244	MEDSIL1035A and MEDSIL1035B	HISIL7262	HISIL9163
Starting material	MEDSIL	MEDSIL	MEDSIL + $CaSiO_3$	MEDSIL + $CaSiO_3$	HISIL	HISIL + diopside
P (GPa)	1.1	1.1	1.1	1.1	1.1	1.1
$T_{initial}$ (°C)	1445	1300	1300	1300	1300	1300
T_{final} (°C)	1150	1150	1155	1150	1145	1145
Time at T_{final} (h)	18.5	0	0	250	0	0
Run products	Cpx, melt	Cpx, opx, melt	Cpx, melt	Cpx, melt	Cpx, melt	Cpx, melt

To assess whether measured partition coefficients were dependent on crystallization path, experiment MEDSIL1035A/B produced cpx crystals by approaching the final temperature from below after undercooling by 20 °C. The temperature was held at 1300 °C for 6 min, stepped to 1200 °C for 5 h, ramped down to 1130 °C and immediately back to 1150 °C at 10 °C/h, where the experiments dwelled for 250 h before quenching.

Run products were mounted in epoxy, sectioned, and polished. The major-element composition of glassy and crystalline phases in all samples except MEDSIL2161 were determined by energy dispersive (EDS) X-ray analysis on the JEOL 840A scanning electron microscope in the Department of Geology, University of Illinois at Urbana-Champaign. The accelerating voltage was 15 kV and the electron beam current was 10 nA. Standards-based EDS analysis used a 4Pi Revolution software system, which includes full ZAF corrections. Measured compositions of secondary standards (Smithsonian standards Tektite Glass and Kakanui Augite) are in good agreement with the reported values for these two standards indicating the accuracy of our measurements (Table 3). Glass analyses were performed by rastering over a ~15 μm square to avoid vaporization of Na, and crystals were analyzed in spot mode (beam diameter ~1 μm). Cpx, orthopyroxene, olivine, and glass analyses for experiment MEDSIL2161 were made using the Cameca SX-50 electron microprobe at the University of Chicago using a 15 kV accelerating voltage and 10 nA beam current with the calibration based on well-characterized mineral and oxide standards.

Trace-element concentrations were determined by Laser Ablation-Inductively Coupled Plasma-Mass Spectrometry (LA-ICP-MS) using a Finnigan ELEMENT 2 ICP-MS coupled to an ArF charged, excimer laser operating at 193 nm or a 5th harmonic Nd: YAG laser (UP-213, New Wave Research) operating at 213 nm in the Department of Geology at the University of Maryland. Trace-element concentrations were determined by normalization of ion intensities to Ca or Ti intensity, then correction to CaO or TiO_2 concentrations determined by SEM-EDS (Table 3). Spot size was generally ~20–30 μm in the glass and as small as 8 μm in crystals. Analyses consisted of ~20 s of background monitoring with the laser off, followed by 10–20 s of laser ablation using a combination magnet and E-scan model (Hamester et al. 1999). In some instances, spectral data were obtained from the first few seconds as the small crystals were ablated rapidly. Calibration was performed relative to NIST 610 with several BCR-2 analyses per day used to check accuracy (Table 4).

Trace-element compositions of MEDSIL5244 were also determined on Au-coated mounts by secondary ionization mass spectrometry (SIMS), using the Cameca IMS 5f in the Center for Microanalysis of Materials of the University of Illinois at Urbana-Champaign. A primary beam of 12.5 keV O^- ions, 17–19 nA current, and ~50 μm diameter was used. Secondary ions were accelerated to 4.5 kV. Standard energy filtering techniques used an energy offset of 50 V and an energy window of ~19 eV. To analyze the ~40 μm crystals in this sample, we imaged the cpx and glass by examining ^{133}Cs and ^{52}Cr ions on the channel plate using the largest field aperture, providing a sharp image of the crystal. We then positioned the sample to the predetermined location where ions passing through the smallest field aperture struck the channel plate. We used this smallest aperture sampling ions coming from within <10 μm region in the central portion of the cpx. Any ions from the surrounding glass entering the detector using this procedure would be indicated by increased ^{133}Cs counts; however, none were observed. Calibration was performed on NIST 610 separately for the respective measurement conditions on glass and crystals. The following isotopes were analyzed and ratioed to ^{30}Si: ^{7}Li, ^{41}K, ^{47}Ti, ^{52}Cr, ^{88}Sr, ^{90}Zr, ^{133}Cs, ^{139}La, ^{143}Nd, ^{147}Sm, ^{151}Eu, ^{159}Tb, ^{167}Er, and ^{174}Yb (Table 4). External precisions for most isotopes (except ^{90}Zr) were better than 15%.

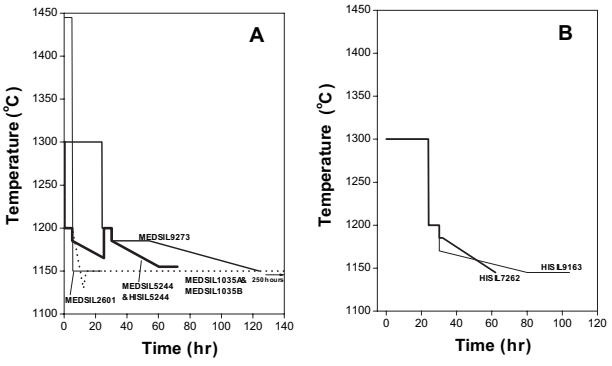

FIGURE 1. (**a**) Time-temperature paths for experiments MEDSIL2601, MEDSIL9273, MEDSIL5244, HISIL5244, MEDSIL1035A, and MEDSIL1035B. (**b**) Time-temperature paths for experiments HISIL7262 and HISIL9163.

RESULTS

Based on visual inspection, all experiments resulted in less than 15% percent crystallization. Mass balance of SiO_2, MgO, CaO, and Al_2O_3 concentrations indicate ~12% crystallization. One representative MEDSIL sample (MEDSIL5244) has 8% cpx by volume based on the measured area of glass and cpx in digital images using NIH image software. Thus, all three techniques indicate low crystallinity such that the concentration of trace elements in the melt did not change appreciably during the crystallization process.

The experimental runs produced diopside crystals up to 70 μm in diameter. Figure 2 shows a back-scattered electron (BSE) image of a representative diopside crystal from experiment MEDSIL5244. Some crystals inevitably contained small melt inclusions. Only euhedral to sub-euhedral crystals without obvious melt inclusions in reflected light were chosen for trace- and major-element analyses. The trace-element contents of glass and cpx crystals in MEDSIL5244 were determined by both LA-ICP-MS and SIMS, allowing direct comparison of the two techniques (Fig. 3). Both partition coefficients and concentrations by the two methods agree within errors and show no systematic bias.

Major-element composition

The compositions of the cpx in this study have a strong resemblance to typical mantle chromian diopsides with high

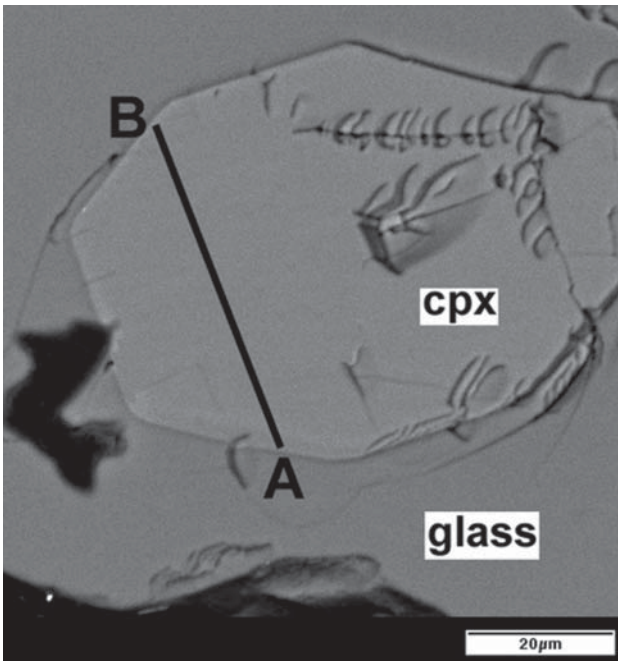

FIGURE 2. Back-scattered electron image of a representative clinopyroxene crystal in sample MEDSIL5244. The line AB represents the analytical traverse shown in Figure 4. The black area near the crystal is due to a polishing problem.

TABLE 3. Major element compositions of clinopyroxenes and glasses

Element	MEDSIL2161				MEDSIL2601		MEDSIL9273		MEDSIL5244	
	Glass(4)	Opx(2)	Ol(1)	Cpx(3)	Glass (5)	Cpx (4)	Glass (4)	Cpx (4)	Glass(12)	Cpx (26)
SiO_2	62.00±37	57.87±62	41.55	54.87±22	63.75±35	53.88±20	63.91±16	54.61±12	63.55±12	54.50±16
Al_2O_3	17.69±22	2.20±29	0.39	3.52±17	17.87±36	4.77±37	17.46±6	3.20±4	16.92±9	3.51±26
FeO	1.38±9	5.80±7	9.63	3.38±4	1.33±3	3.34±10	1.34±6	2.48±10	1.70±6	1.91±21
MgO	1.47±6	30.8±1.3	47.55	18.14±69	1.80±7	17.63±29	1.97±2	19.11±30	2.29±4	16.69±38
CaO	0.91±2	2.31±57	0.17	17.23±57	0.96±5	18.39±69	1.64±7	19.06±47	2.82±5	22.06±27
Na_2O	5.78±12	0.24±3	0.13	1.28±4	5.45±6	1.37±7	4.74±9	1.01±2	4.64±9	0.99±5
K_2O	8.00±12	0.06±1	0.20	0.12±12	8.36±5	0.08±1	7.95±9	0.04±4	7.60±7	0.04±2
TiO_2	0.39±7	0.16±6	0.01	0.30±6	0.49±4	0.47±13	1.00±2	0.49±3	0.48±3	0.25±6
Cr_2O_3	–	–	–	–	–	0.10±6	–	–	–	0.05±4
Total	97.68	99.22	99.63	98.85	100	100	100	100	100	100
X_{Mg}	0.66	0.90	0.90	0.91	0.71	0.90	0.72	0.93	0.71	0.94
NBO/T	0.11				0.12		0.12		0.17	
$Ca^{2+}/(M^{2+}+M^{+})$	0.0379				0.0395		0.0699		0.1138	
Cations in clinopyroxene in a 6 oxygen basis										
Site	Cation									
IV	Si^{4+}			1.983		1.934		1.955		1.961
	Al^{3+}			0.017		0.066		0.045		0.039
M1	Mg^{2+}			0.757		0.749		0.822		0.824
	Al^{3+}			0.132		0.136		0.090		0.110
	Ti^{4+}			0.008		0.013		0.013		0.007
	Cr^{3+}			0.000		0.003		0.000		0.001
	Fe^{2+}			0.102		0.100		0.074		0.057
M2	Ca^{2+}			0.667		0.707		0.731		0.851
	Na^{+}			0.090		0.095		0.070		0.069
	K^{+}			0.006		0.003		0.002		0.002
	Mg^{2+}			0.220		0.195		0.197		0.071
	Total			3.98		4.00		4.00		3.99
Component in clinopyroxene										
Jd				0.090		0.095		0.070		0.069
TiTs				0.008		0.013		0.013		0.007
CaTs				0.022		0.041		0.020		0.033
*D*i				0.637		0.654		0.698		0.811
EnFs				0.221		0.195		0.198		0.071
Total				0.98		1.00		1.00		0.99

Notes: The relative error on NBO/T is less than 2% based on the errors of major element analyses of the glasses. NBO/T is calculated after Mysen et al. (1985). Numbers in parentheses denote number of analyses. 53.88 ± 20 should be read as 53.88 ± 0.20. The errors are based on one standard deviation of the analysis population. All data except MEDSIL2161 were measured by SEM-*EDS*. MEDSIL2161 measured by electron probe microanalysis (EPMA) at the University of Chicago.

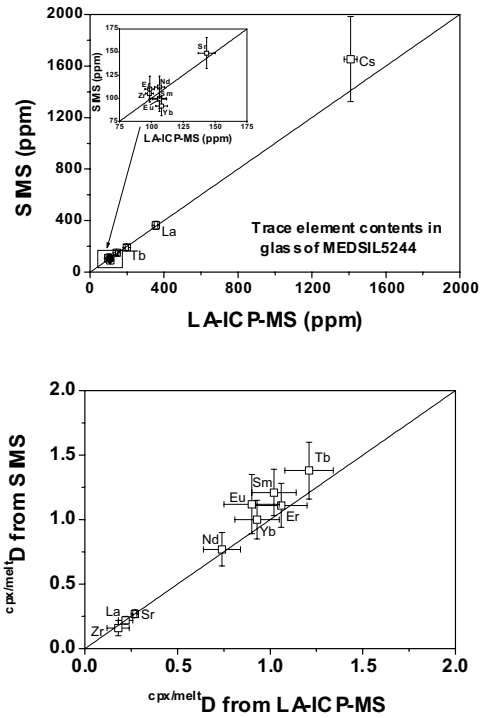

FIGURE 3. Comparison of trace-element contents of glass and partition coefficients of MEDSIL5244 as determined by LA-ICP-MS and SIMS methods.

SiO_2, CaO, MgO, and low Al_2O_3 contents. Values of X_{Mg} in these crystals range from 0.90 to 0.94, and Al_2O_3 and Na_2O contents are 3.20–5.11 and 0.92–1.37 wt%, respectively (Table 3). Indeed, experiment MEDSIL2161 shows that the MEDSIL melt is near multiple saturation in olivine, orthopyroxene, and cpx, all with X_{Mg} ~0.9, typical of most upper-mantle peridotite samples.

Cpx in the experiments are zoned slightly. A compositional traverse across a representative cpx crystal in MEDSIL5244 (line AB in Fig. 3) is shown in Figure 4a. Concentrations of SiO_2, CaO, and MgO are relatively invariant across the cpx crystal. Al_2O_3 is slightly zoned, with higher Al_2O_3 contents in the core than the rim. Similar zoning of Al_2O_3 was reported in diopsides in Lundstrom et al. (1994); because Al_2O_3 is incompatible in cpx, Al_2O_3-rich cores cannot be due to enrichment at the crystal-melt interface. The variations in Na_2O, FeO, and TiO_2 concentration across the cpx are small.

The average major-element compositions of cpx and glasses in eight experiments are given in Table 3. Cpx and melt compositions in MEDSIL experiments closely follow those in the experiments of Draper and Green (1999) (Table 3). Glass compositions in HISIL experiments have higher SiO_2 than MEDSIL experiments, resembling the silicic glass observed in a harzburgite xenolith (PAT2-68) from Vannucci et al. (1998).

The ratio of non-bridging O atoms to tetrahedrally coordinated cations (NBO/T) has been used extensively to quantify silicate melt polymerization (Mysen and Virgo 1980; Mysen et al. 1985). As melt polymerization increases, NBO/T decreases

TABLE 3. —*Continued*

Element	MEDSIL1035A		MEDSIL1035B		HISIL7262		HISIL9163		HISIL5244	
	Glass(6)	Cpx(6)	Glass(6)	Cpx(6)	Glass (4)	Cpx (4)	Glass(4)	Cpx (5)	Glass(5)	Cpx(5)
SiO_2	62.76±14	54.02±7	64.17±14	54.34±26	69.44±58	53.00±49	68.97±6	54.30±22	69.35±10	53.52±14
Al_2O_3	17.29±9	2.88±36	17.65±7	3.49±46	15.89±27	5.11±41	16.26±5	4.39±36	15.94±8	4.40±10
FeO	1.76±2	1.95±28	1.51±8	2.64±39	1.34±1	3.68±43	1.20±5	2.51±24	1.44±4	3.32±20
MgO	2.37±4	17.47±20	2.04±5	18.81±27	1.94±5	18.84±71	1.57±4	18.28±57	1.72±2	18.21±14
CaO	2.92±3	22.60±43	1.84±2	19.43±48	2.61±5	16.38±85	1.76±1	17.99±70	2.45±9	18.07±26
Na_2O	5.05±10	0.92±9	4.80±6	1.01±5	4.29±23	1.04±5	5.10±1	1.17±5	4.29±10	1.01±04
K_2O	7.47±5	0.11±4	7.60±9	0.11±4	4.33±10	0.01±2	4.68±2	0.01±1	4.22±4	0.08±3
TiO_2	0.38±5	0.11±4	0.40±4	0.19±9	0.16±5	0.17±5	0.48±3	0.42±6	0.60±9	0.36±4
Cr_2O_3	–	–	–	–	–	1.77±28	–	0.94±15	–	1.02±9
Total	100	100	100	100	100	100	100	100	100	100
X_{Mg}	0.71	0.94	0.71	0.93	0.72	0.90	0.70	0.93	0.68	0.91
NBO/T	0.18		0.13		0.10		0.08		0.13	
$Ca^{2+}/(M^{2+}+M^{+})$	0.1139		0.0779		0.1342		0.0894		0.0131	
Cations in clinopyroxene in a 6 oxygen basis										
Site	Cation									
IV	Si^{4+}	1.951		1.950		1.955		1.941		1.924
	Al^{3+}	0.049		0.050		0.045		0.059		0.076
M1	Mg^{2+}	0.864		0.819		0.822		0.761		0.751
	Al^{3+}	0.074		0.098		0.090		0.126		0.111
	Ti^{4+}	0.003		0.004		0.013		0.011		0.010
	Cr^{3+}	0.000		0.000		0.000		0.027		0.029
M2	Fe^{2+}	0.875		0.747		0.074		0.075		0.696
	Ca^{2+}	0.064		0.070		0.731		0.689		0.071
	Na^{+}	0.003		0.005		0.070		0.081		0.003
	K^{+}	0.076		0.187		0.002		0.000		0.225
	Mg^{2+}	0.875		0.747		0.197		0.212		0.696
	Total	4.02		4.01		4.00		3.98		4.00
Component in clinopyroxene										
Jd		0.064		0.070		0.073		0.081		0.071
TiTs		0.003		0.004		0.005		0.011		0.010
CaTs		0.026		0.034		0.067		0.040		0.048
Di		0.845		0.708		0.558		0.637		0.638
EnFs		0.077		0.188		0.280		0.206		0.219
Total		1.02		1.01		0.98		0.98		0.99

Element	PAT2-68		DGA-44*		Tektite glass		Kakanui augite	
	Glass	Cpx	Glass	Cpx	True	This study	True	This study
SiO_2	69.06±1.56	54.97±31	60.96±23	54.69±63	75.75	76.17	50.73	50.53
Al_2O_3	16.94±79	0.59±18	18.38±11	3.52±78	11.34	11.35	8.73	8.79
FeO	1.74±21	2.74±17	1.48±9	3.66±37	4.90	4.56	6.44	6.51
MgO	1.15	18.10±27	1.91±5	19.92±1.27	1.51	1.68	16.65	16.15
CaO	1.32±22	21.59±50	1.63±6	16.70±1.09	2.66	2.70	15.82	16.05
Na_2O	4.92±1.11	0.76±17	5.99±15	0.99±14	1.06	1.19	1.27	1.26
K_2O	4.64±52	0.01	7.32±22	–	1.88	1.83	0.00	0.00
TiO_2	0.08±0	–	0.38±5	0.58±12	0.50	0.52	0.74	0.71
Cr_2O_3	–	1.28±31	–	–	–	–	0.14	
Total	99.91	100.05	98.05	100.13	99.60	100	100.52	100
X_{Mg}	0.92		0.91					
NBO/T	0.13		0.08		0.10		0.08	
$Ca^{2+}/(M^{2+}+M^{+})$								
Cations in clinopyroxene in a 6 oxygen basis								
Site	Cation							
IV	Si^{4+}	1.991		1.952				
	Al^{3+}	0.009		0.048				
M1	Mg^{2+}	0.864		0.775				
	Al^{3+}	0.016		0.100				
	Ti^{4+}	0.000		0.016				
	Cr^{3+}	0.037		0.000				
M2	Fe^{2+}	0.083		0.109				
	Ca^{2+}	0.838		0.639				
	Na^{+}	0.053		0.069				
	K^{+}	0.000		0.000				
	Mg^{2+}	0.113		0.285				
	Total	4.00		3.99				
Component in clinopyroxene								
Jd		0.053		0.069				
TiTs		0.000		0.016				
CaTs		0		0.024				
Di		0.852		0.599				
EnFs		0.104		0.285				
Total		1.01		0.99				

* *D*GA-44 is from Draper and Green (1999).

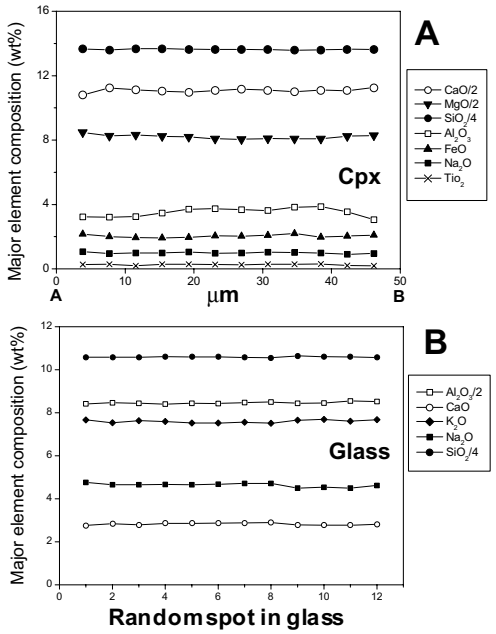

FIGURE 4. Profiles of major-element compositional variations in clinopyroxene and glass. (**a**) Variation in composition of clinopyroxene across the analytical traverse AB in Figure 2. The clinopyroxenes show minor zoning in major elements and moderate zoning in Al_2O_3. The Al_2O_3 profile argues against boundary layer development at the melt-clinopyroxene interface because Al is incompatible in the clinopyroxene. (**b**) Variation in glass composition among 12 random spots. No variations outside of analytical errors are detectable.

due to the decrease in non-bridging O atoms and increased in molar SiO_2 content. The melts in our study (Table 3) have a higher degree of melt polymerization than those in most previous cpx-silicate melt partitioning studies (e.g., Hart and Dunn 1993; Johnson 1998; Lundstrom et al. 1998; Salters and Longhi 1999). The NBO/T of MEDSIL and HISIL experiments range from 0.11–0.18 and 0.08–0.13, respectively.

Evaluation of equilibrium and Henry's Law behavior

Determining equilibrium partition coefficients requires that the melt remains chemically homogeneous as the crystals grew and that no boundary layer of element enrichment or depletion occurred at the interface between the growing crystal and the melt. Several observations indicate that our measured partition coefficients represent equilibrium values independent of the *P-T* path. First, in all experiments, glass compositions are homogeneous for major and trace elements within the errors of the analyses (Fig. 4b), excepting subtle Al_2O_3 zoning in cpx mentioned above. Second, the low values for D_K and D_{Cs} in experiment MEDSIL5244 argue that neither analytical problems nor non-equilibrium bias the partition coefficients toward unity. The concentration of Cs in cpx in MEDSIL5244 is at the detection limit of the ion microprobe analysis, requiring a maximum value of ${}^{cpx/melt}D_{Cs}$ of 5×10^{-4}, and the partition coefficient for K is similar to other cpx-melt determinations (e.g., 0.04–0.004 in Hack et al. 1994; 0.015–0.045 in Johnson 1998; 0.027 in Pertermann and Hirschmann 2002). The experiment with highest ${}^{cpx/melt}D_{REE}$ (MEDSIL2601) has a low K_2O content (0.08 wt%), similar to other experiments, precluding bulk enrichment in all incompatible elements by fast non-equilibrium growth. Finally, the high values of ${}^{cpx/melt}D_{HREE}$ are unlikely to be due to disequilibrium effects or glass contamination because these partition coefficients are greater than one and incorporation of glass or fast crystal growth should result in a lower concentration in the solid than that for the equilibrium partition coefficient.

Experiment MEDSIL1035A/B demonstrates that our measured partition coefficients are independent of crystallization path and therefore represent a close approach to equilibrium. MEDSIL10035A and MEDSIL5244 represent identical starting materials (Table 2) run under identical final *P-T* conditions but having very different time-temperature paths. The partition coefficients of MEDSIL1035A and MEDSIL5244 are within error for all elements except Sr, which is slightly outside of error (Table 4).

Finally, we show later that our measured ${}^{cpx/melt}D_{REE}$, along with those from a previous study identifying melt structure control (Gaetani 2004), correlate well with a parameter of melt structure $Ca^{2+}/(M^+ + M^{2+})$ [M^+ and M^{2+} denote the moles of monovalent (i.e., Na^+, K^+) and divalent (i.e., Ca^{2+}, Mg^{2+}, Fe^{2+}) cations in the melt, respectively]. This observation, along with the consistency of Zr and Sr partition coefficients with previous experimental and phenocryst-glass studies (Green and Pearson 1985; Watson and Ryerson 1986; Skulski et al. 1994; Lundstrom et al. 1994, 1998; Chazot et al. 1996; Hill et al. 2000; Vannucci et al. 1998), argues for the robustness of our results.

Adherence to Henry's Law behavior is indicated by two observations. First, the total dopant level (<0.5 wt%) is well below the anticipated upper limits of Henry's Law behavior demonstrated by several previous studies (Watson 1985; McKay 1986), including previous cpx-melt studies (Ray et al. 1983; Lundstrom et al. 1994). Second, experiment MEDSIL1035A/B provided a direct assessment of Henry's law, with La, Tb, and Yb doped at 2× higher concentrations in MEDSIL1035B relative to MEDSIL1035A. However, for reasons probably relating to nucleation as a function of dopant addition, MEDSIL1035B had a significantly higher degree of crystallinity, resulting in a lower CaO content in the melt. As we will show, the observed partitioning difference between these experiments is completely explained by the difference in the $Ca^{2+}/(M^+ + M^{2+})$ of the two melts.

Incorporation of surrounding glass or melt inclusions into the crystal during trace-element analysis would strongly bias partition coefficients for highly incompatible elements. We therefore use Cs concentrations in cpx as a monitor of the maximum contribution of glass contamination on the measured partition coefficients. Given Cs concentrations in cpx are below the LA-ICP-MS detection limit (~2.3 ppm with crater size of 10 μm) and Cs melt concentrations >160 ppm, the effect of glass contamination on the partition coefficients on any experiment must be less than that in the highest measured ${}^{cpx/melt}D_{Cs}$ (0.02 in HISIL9163). Therefore, assuming ${}^{cpx/melt}D_{Cs} = 0$, the maximum contribution from glass contamination to the cpx analysis of any other incompatible element is 0.02 or 2%. Thus, glass contamination will change partition coefficients by <10% for trace elements with ${}^{cpx/melt}D > 0.2$, whereas generally within the measurement error and becoming less significant with increasing ${}^{cpx/melt}D$. Most partition coefficients reported here are >0.2 (Table 4), making

TABLE 4. Trace element concentrations (ppm) of glass and clinopyroxene/melt partition coefficients

Sample	MEDSIL2601*			MEDSIL9273*			MEDSIL5244†			MEDSIL5244*			MEDSIL1035A*		
Element	Cpx	Glass	$^{Cpx/melt}D$	Cpx	Glass	$^{Cpx/melt}D$	Cpx	Glass	$^{Cpx/melt}D$	Cpx	Glass	$^{Cpx/melt}D$	Cpx	Glass	$^{Cpx/melt}D$
Na			0.25(1)			0.21(1)			0.21(1)						0.18(2)
Mg			9.8(4)			9.7(2)			7.3(2)						7.4(1)
Al			0.27(2)			0.18(0)			0.21(2)						0.17(2)
Ca			19.1(1.2)			11.7(6)			7.8(2)						7.7(2)
Ti			0.97(29)			0.49(3)			0.53(13)						0.28(12)
K‡									0.030(16)						
Cr							824(96)	30.3(4.3)	27(5)						
Li							9.8(2.3)	61.9(5.7)	0.16(4)				12.0(2.4)	48.2(5.1)	0.25(6)
Sr							40.4(2.4)	149(17)	0.27(3)	39.8	143(7)	0.27(1)	57.8(2.5)	150(29)	0.39(9)
Zr				19.7(0)	84.4(4.5)	0.23(1)	16.3(6.4)	105(6)	0.16(6)	17.8(6.0)	98.4(3)	0.18(6)	13.7(5.5)	79.4(4.6)	0.14(6)
Cs								1653(330)	$<5\times10^{-4}$		1408(34)				
La	112(6)	167(6)	0.67(9)	106(7))	324(3)	0.33(2)	80.4(7.9)	363(32)	0.22(3)	77.6(14.0)	355(10)	0.22(4)	71.9(11.6)	325(13)	0.22(5)
Nd	284(29)	138(4)	2.06(18)	101(14)	86.9(1.0)	1.16(16)	86(11)	112(12)	0.77(13)	79(10)	106(4)	0.74(10)	72.3(8.9)	101(5)	0.71(13)
Sm	384(22)	125(18)	3.06(51)	140(26)	83.0(4.4)	1.69(33)	121(11)	100(11)	1.21(18)	108(12)	106(5)	1.02(12)	92.6(12.9)	95.0(6.8)	0.99(20)
Eu	361(7)	136(6)	2.65(24)	99(21)	77.4(1.7)	1.28(27)	110(18)	99(13)	1.12(23)	96(15)	106(6)	0.90(15)	82.8(11.3)	94.1(6.5)	0.88(18)
Tb							265(30)	192(23)	1.38(22)	241(22)	199(9)	1.21(13)	214(28)	187(12)	1.14(22)
Er	371(5)	115(18)	3.21(57)	243(27)	77.7(3.2)	3.12(37)	123(12)	110(14)	1.11(17)	104(13)	99(4)	1.06(14)	91.5(13.7)	93.5(8.7)	0.98(22)
Yb	351(18)	130(14)	2.69(40)	213(19)	81.8(3.7)	2.61(21)	91(10)	91.4(10.2)	1.00(15)	100(12)	108(5)	0.93(12)	88.9(11.6)	105(5)	0.85(16)

Sample	MEDSIL1035B*			HISIL7262*			HISIL9163*			HISIL5244*			BCR-2G*
Element	Cpx	Glass	$^{Cpx/melt}D$	Cpx	Glass	$^{Cpx/melt}D$	Cpx	Glass	$^{Cpx/melt}D$	Cpx	Glass	$^{Cpx/melt}D$	
Na			0.21(1)			0.24(2)			0.23(1)			0.23(1)	
Mg			9.2(3)			9.7(4)			11.7(5)			10.6(2)	
Al			0.20(3)			0.32(3)			0.27(2)			0.28(1)	
Ca			10.6(3)			6.27(35)			10.2(4)			7.4(3)	
Ti			0.40(22)			1.04(42)			0.87(13)			0.59(11)	
K‡													
Cr													
Li													
Sr							18.4(2.9)	79.1(2.1)	0.23(4)				297
Zr	14.4(4.2)	103(9)	0.14(4)				16.8(1.2)	81.1(3.8)	0.21(2)	30(12)	160(26)	0.19(9)	170
Cs							15(1)	662(11)	0.023(2)				0.91
La	152(4)	586(37)	0.26(3)	26.0(0.7)	200(7)	0.13(4)	43.5(4.6)	203(3)	0.21(3)	39.3(9.4)	285(10)	0.14(4)	21
Nd	129(16)	123(7)	1.05(18)	56.9(2.4)	139(6)	0.41(13)	61.0(7.4)	70.0(1.6)	0.87(12)	50.4(10.1)	74.8(6.7)	0.67(18)	23
Sm	189(20)	118(23)	1.61(39)	70.6(3.9)	93(10)	0.76(25)	61(11)	42.7(1.2)	1.43(28)	49.9(8.6)	50.5(3.2)	0.99(23)	5.67
Eu	130(15)	115(8)	1.23(19)	37(11)	201(13)	0.19(8)	47.2(1.1)	92.7(3.1)	0.51(4)	96(19)	101(5)	0.95(24)	1.76
Tb	433(15)	232(50)	1.86(44)							315(26)	186(9)	1.69(30)	
Er	212(13)	116(18)	1.82(35)	141(7)	122(8)	1.15(36)	100(1)	54.5(1.3)	1.83(12)	102(13)	62.2(1.5)	1.64(33)	2.99
Yb	415(36)	260(42)	1.60(33)	192(16)	200(3)	0.96(30)	132(7)	85.1(4.5)	1.55(15)	148(27)	93.3(6.9)	1.59(39)	2.82

Notes: The numbers in parentheses represent one standard deviation based on 3–5 analyses, e.g., 0.25(1) should be read as 0.25 ± 0.01 and 19.1(1.2) as 19.1 ± 1.2.
* Measured using LA-ICP-MS at the University of Maryland.
† Measured using SIMS at the University of Illinois at Urbana and Champaign. Estimation of D_{Cs} of DRA5244 is based on the detection limit of the ion probe analysis for the conditions of analysis.
‡ Because K_2O contents in clinopyroxene are under the detection limit of EDS analysis method, only $^{cpx/melt}D_K$ of *D*RA5244 determined by SIMS is listed.

glass contamination effects insignificant to our conclusions. Although several incompatible elements (Rb, Ba, Nb, Hf, Ta, Pb, Th, and U) were also doped into the starting material, partition coefficient data for these elements are not reported because of the limited ability to quantify these elements in small spot analyses or because glass contamination may have significantly affected measured partition coefficients.

Partition coefficients and comparison with previous results

Cpx-melt partition coefficients for Ti, K, Li, Cr, Sr, Zr, and REE are given in Table 4. The patterns of partition coefficients of REE for MEDSIL5244, MEDSIL1035A, and HISIL5244, representative of the two different compositions, are shown in Figure 5. For comparison, $^{cpx/melt}D$ from Blundy et al. (1998) and Vannucci et al. (1998) are also shown in Figure 5. The eight experiments in this study produce similar patterns for the REE partition coefficients with a maximum partition coefficient occurring in the middle REE (MREE), usually Tb. Heavy REE (HREE) are compatible (but $D_{HREE} < D_{MREE}$) whereas light REE (LREE) are incompatible. D_{Eu} shows a negative anomaly relative to Sm and Tb, or Er, consistent with the presence of significant amounts of Eu^{2+} in the experiment due to the relatively reducing conditions of graphite capsules (Ulmer and Luth 1991). Notably, HISIL composition samples consistently show larger Eu anomalies than MEDSIL samples despite the fact that all experiments were run under ostensibly the same f_{O_2}.

Compared to studies using natural basaltic starting material, our measured partition coefficients are significantly larger, including the REE partition coefficients of Blundy et al. (1998), representing the upper limit of experimentally determined $^{cpx/melt}D$. Although $^{cpx/melt}D_{HREE}$ in Blundy et al. (1998) are greater than one, similar to those here, $^{cpx/melt}D$ of the MREE and LREE were significantly lower than the values in this study (Fig. 5). Thus, a significant difference between this study and that of Blundy et al. (1998) is the fact that the D_{REE} patterns here peak near the MREE while the Blundy et al. (1998) partition coefficients peak at Lu. The partition coefficients for REE in this study are significantly larger than partition coefficients between cpx and basaltic or andesitic melts (Skulski et al. 1994; Lundstrom et al. 1998; Hill et al. 2000). For instance, the average $^{cpx/melt}D_{La}$ of these previous studies was 0.062 vs. 0.27 here while the average $^{cpx/melt}D$ of Yb was 0.34 vs. 1.6 here.

Although partition coefficients derived from measurements of coexisting mineral and glasses in natural samples can have uncertainties associated with establishment of equilibrium, there is remarkable agreement between our results and those from the diopside-silica rich glass analyses of a harzburgite xenolith in Vannucci et al. (1998). First, their study found MREE and HREE partition coefficients greater than one with the maximum partition coefficient occurring in the MREE, and D_{REE} correlating with NBO/T. Second, although D_{Ti} was significantly elevated relative to cpx-basaltic melt partitioning, D_{Zr} was not. Finally, $^{cpx/melt}D_{Sr}$ (0.23–0.39) was also elevated significantly over typical cpx-basalt values (Vannucci et al. 1998). All of these observations, including the partitioning of Ti-Zr-Sr relative to the REE as well as the absolute partition coefficients, are in agreement with our experimentally determined diopside-silicic melt partition coefficients.

Discussion

The cpx-melt partition coefficients measured here, particularly those for the REE, are among the highest yet determined experimentally. As explained below, none of the obvious crystal-chemical controls appear to explain these large partition coefficients. Our discussion focuses on understanding the reasons for this element partitioning behavior leading to the conclusion that this dominantly reflects melt structure. We follow this with a section applying our results to observed cpx compositions in upper-mantle samples providing evidence for the existence of high-silica melt at the shallow depths (<1.0 GPa) in the upper mantle.

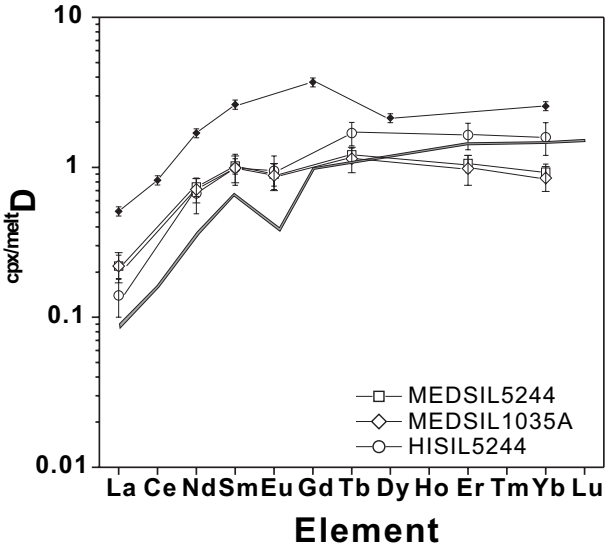

Figure 5. Clinopyroxene-melt partition coefficients of REE of MEDSIL5244 (measured by LA-ICP-MS), MEDSIL1035A, and HISIL5244 compared to data from Blundy et al. (1998) (gray line), inferred diopside-silicic glass partitioning in xenolith PAT2-68 (small solid diamond) from Vannucci et al. (1998). Error bars reflect one standard deviation. The data from Blundy et al. (1998) represent the upper limit of partition coefficients using basaltic starting material.

Lattice strain model

The lattice strain model has been widely applied to trace-element partitioning studies of the past 10 years. This model, based on the work of Brice (1975), suggests that the partitioning of an element between a mineral and melt depends on the elastic strain energy generated by the misfit in size of the ion relative to the ideal ionic radii of an ion entering that site (Blundy and Wood 1994, 2003; Wood and Blundy 1997). The lattice strain model of Blundy and Wood (1994) can be used to calculate the ideal ionic radius (r_0), Young's modulus (E), and optimum D (D_0) for a set of isovalent cations by fitting a parabolic curve of the partition coefficients as a function of the ionic radii (e.g., an Onuma diagram). Blundy and Wood (1994) described the partition coefficient D_i of an element i by:

$$D_i = D_0 \exp\left(\frac{-4\pi E N_A [r_0(r_i - r_0)^2/2 + (r_i - r_0)^3/3]}{RT}\right) \quad (1)$$

where r_i is the ionic radii, N_A is Avogadro's number, R is the gas constant, and T is the temperature in K (Blundy and Wood 1994). According to the lattice strain model, a set of isovalent cations entering the same site in a mineral will experience the same r_0, E, and D_0 with D_i decreasing as the difference between r_i and r_0 increases.

We performed a weighted non-linear least squares fit to Equation 1 providing results for r_0, E, and D_0 for each experiment (Table 5). A representative sample (MEDSIL5244) is shown with a corresponding fit parabola (Fig. 6). The r_0 in these experiments (1.01–1.04 Å) is shifted to higher values compared to most cpx-melt studies (e.g., 0.981 Å of Blundy et al. 1998; or 0.992 Å of Lundstrom et al. 1998). Because melt structure does not discriminate the relative partitioning of the REE (Ryerson and Hess 1978), this shift must reflect crystal chemical control, specifically, the high Na_2O and CaO and low Al_2O_3 contents of the cpx. This result follows that of Bennett el al. (2004), who found that the Na bearing cpx from their NCMAS experiment had higher r_0 than that in their CMAS experiment reflecting the effect of Na^+ on M2 site size.

Table 5. r_0, Young's modulus, and D_0 for +3 cations in the M2 site for different experiments using lattice strain model of Blundy and Wood (1994)

Source	N*	r_0 (Å)	R^2	E_M (GPa)	D_0
MEDSIL2601	5	1.039(1)	1.000	320(5)	3.62(3)
MEDSIL9273	5	1.006(10)	0.995	255(37)	2.86(16)
MEDSIL5244†	6	1.041(2)	0.996	366(18)	1.39(4)
MEDSIL5244	6	1.039(2)	0.998	328(13)	1.23(2)
MEDSIL1035A	6	1.041(1)	0.999	328(10)	1.16(2)
MEDSIL1035B	6	1.033(3)	0.996	353(22)	2.02(6)
HISIL7262	5	1.013(9)	0.994	281(39)	1.09(6)
HISIL9163	5	1.029(0)	1.000	363(3)	1.95(1)
HISIL5244	6	1.015(6)	0.996	335(30)	1.72(7)
*Di*An‡	4	1.03	0.992	297.9	0.30
*Di*Ab‡	4	1.03	0.999	292.4	0.27
4EHE§	13	1.01	0.828	256	0.81
93PC26‖	3	1.05	–	395.6	–

* *N* is number of elements used for calculation.
† Calculated from data measured by SIMS.
‡ *Di*An and *Di*Ab from Lundstrom et al. (1998).
§ 4EHE from Hill et al. (2000).
‖ 93PC26 from Blundy and Wood (1994).

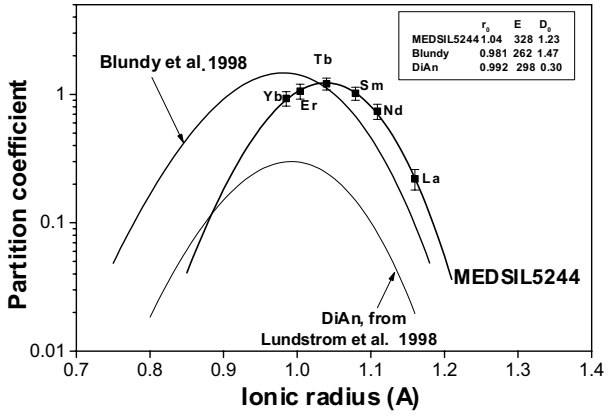

FIGURE 6. Variation in $^{cpx/melt}D$ for experiment MEDSIL5244 as a function of ionic radius. $^{cpx/melt}D$-ionic radii curves represent parabolas calculated from the lattice strain model (Blundy and Wood 1994) using r_0, E, and D_0 obtained from linear fits (Table 5; see text). For comparison, the parabolas for +3 cations of the experiment of Blundy et al. (1998) and DiAn experiment of Lundstrom et al. (1998) are also shown; note the offset of the parabola peak observed here to larger ionic radii relative to the parabolas of Blundy et al. (1998) and Lundstrom et al. (1998). Ionic radii (Å) of cations in eightfold coordination are from Shannon (1976).

The effect of crystal composition on cpx-melt partitioning

Assessing the relative importance of different controls on trace-element partitioning is made difficult by the fact that many of these parameters are intimately linked. For example, polymerized melts often contain high Na_2O contents, which in turn result in relatively high Na_2O contents within coexisting minerals. Here, we attempt to identify the most important controls under specific conditions, with the ultimate goal being a parameterization of cpx-melt partitioning that can account for these entangling effects. The cpx crystals in this study are diopsidic with low Al_2O_3 contents, similar to many previous studies of partitioning with basaltic melts. Thus, comparison of our data with these previous studies should provide a good opportunity to isolate the effects of crystal composition from those of melt structure on trace-element partitioning.

Effect of ^{IV}Al in cpx

Several studies have indicated that cpx-melt partitioning of high-valence trace elements depends on the ^{IV}Al content of cpx (Lundstrom et al. 1994, 1998; Gaetani and Grove 1995; Hill et al. 2000; Pertermann and Hirschmann 2002; Blundy and Wood 2003; Bennett et al. 2004). Hill et al. (2000) demonstrated that the partition coefficients of tri-, tetra-, and pentavalent cations all increase with increasing ^{IV}Al content of the cpx. For instance, $^{cpx/}$

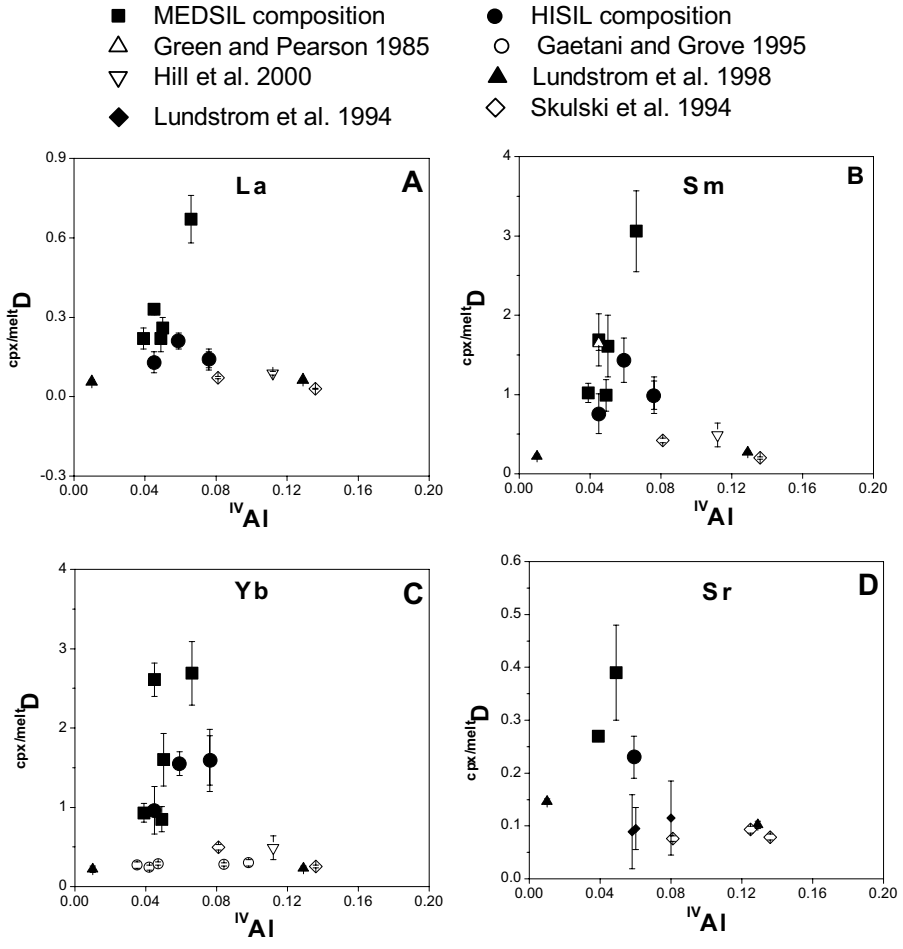

FIGURE 7. $^{cpx/melt}D$ of La, Sm, Yb, and Sr as a function of ^{IV}Al of the clinopyroxene. Other partition coefficients for clinopyroxene with ^{IV}Al < 0.2 are from Green and Pearson (1985), Skulski et al. (1994), Lundstrom et al. (1994, 1998), Gaetani and Grove (1995), and Hill et al. (2000). Although several studies have suggested that ^{IV}Al is a major control on the partitioning of +3 and +4 cations into clinopyroxene (Lundstrom et al. 1994; Hill et al. 2000), there is no relationship observed in these data. Indeed, the highest partition coefficients are observed in the experiments with the lowest ^{IV}Al.

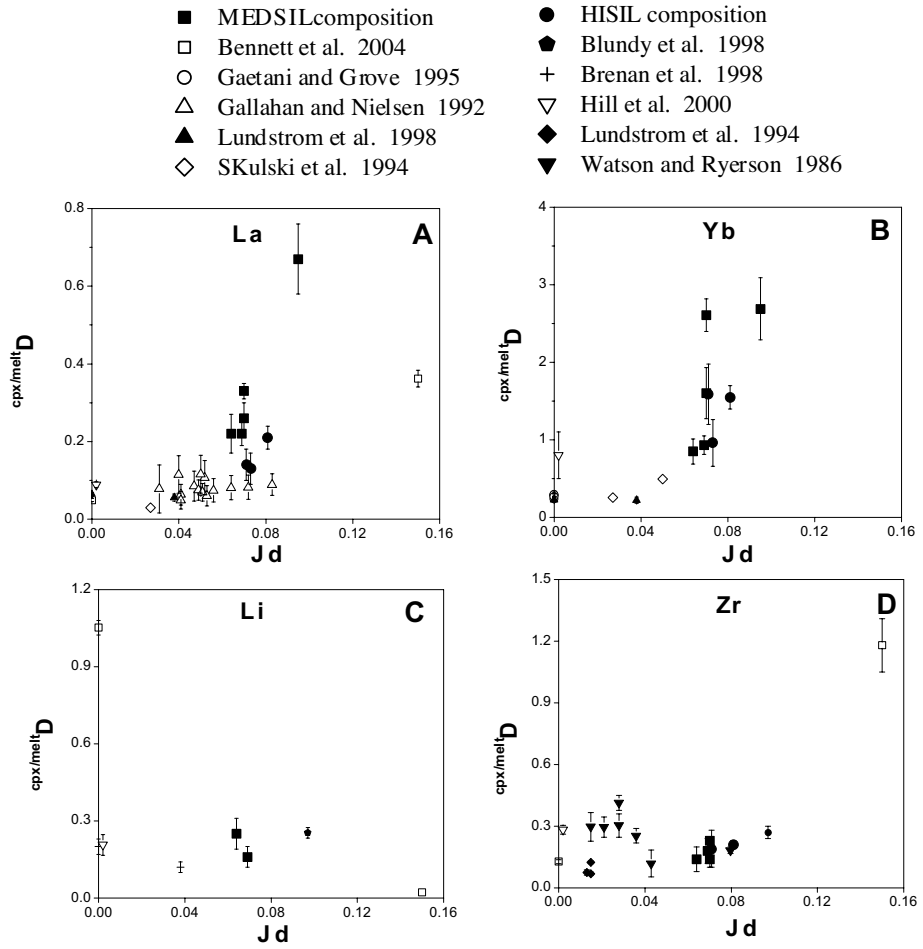

FIGURE 8. $^{cpx/melt}D$ for La, Yb, Li, and Zr as a function of jadeite component in clinopyroxene. Data are from Watson and Ryerson (1986), Gallahan and Nielsen (1992), Skulski et al. (1994), Lundstrom et al. (1994, 1998), Gaetani and Grove (1995), Blundy et al. (1998), Brenan et al. (1998), Hill et al. (2000), and Bennett et al. (2004). All clinopyroxenes except those from Blundy et al. (1998) and Bennett et al. (2004) have high diopsidic component (more than 60 mol%) and low Al_2O_3 contents (no more than 5.8 wt%). The partition coefficients of REE increase with jadeite component in clinopyroxene; however, unlike Bennett et al. (2004), no increase in D_{Zr} or decrease in D_{Li} with jadeite component is observed. Based on the cation distribution in clinopyroxene on a 6 oxygen basis, components in clinopyroxne were obtained using the following sequence: Jd (Jadeite, $NaAlSi_2O_6$) = Na^+, TiTs (Ti-Tschermak, $CaTiAl_2O_6$) = Ti^{4+}, CaTs (Ca-Tschermak, $CaAl_2SiO_6$) = $(Al^{4+}{}_{Total} - Jd - 2TiTs)/2$, *D*i (diopside, $CaMgSi_2O_6$) = Ca^{2+} – CaTs – TiTs, and EnFs [enstatite-ferrosilite solution, $(MgFe)_2Si_2O_6$] = $(Mg^{2+}{}_{Total} + Fe^{2+} - Di)/2$. Our experiments were performed at a reduced environment, so Fe^{3+} in cpx is insignificant.

$^{melt}D_{Ti}$ and $^{cpx/melt}D_{REE}$ positively correlate with ^{IV}Al, with the HREE becoming nearly compatible in ^{IV}Al-rich cpx (Hill et al. 2000). Note that Hill et al. (2000) showed that ^{IV}Al does not significantly affect REE partitioning until ^{IV}Al is greater than 0.1.

In this study, Al_2O_3 contents in cpx range from 3.2 to 5.1 wt%, resulting in ^{IV}Al varying from 0.017 to 0.066, significantly lower than the value at which ^{IV}Al begins to influence REE partitioning (e.g., Hill et al. 2000). There is no correlation between $^{cpx/melt}D_{REE}$ and ^{IV}Al for all experiments with cpx having >65 mol% diopside component and ^{IV}Al <0.20 (Fig. 7). Indeed, from this study, the cpx with some of the lowest ^{IV}Al contents have the highest REE partition coefficients. Therefore, ^{IV}Al does not explain the large REE partition coefficients of our experiments.

Effect of the jadeite content of cpx

Several previous studies have suggested that the jadeite content of cpx might have an important effect on cpx-melt partitioning of trace elements (Blundy et al. 1998; Bennett et al. 2004). Because the Na_2O contents of cpx in this study are up to 1.37 wt%, the effect of Na on the partitioning of trace elements into cpx needs consideration. By comparing partition coefficients from CMAS vs. NCMAS experiments, Bennett et al. (2004) suggested that increasing jadeite component led to increasing $^{cpx/melt}D$ for REE and Zr but decreasing $^{cpx/melt}D_{Li}$. As observed in Figure 8, D_{REE} of this study do increase with jadeite component, consistent with the Bennett et al. (2004) suggestion. However, based on several lines of reasoning, we argue against the high D_{REE} observed here solely reflecting increased jadeite component. First, in contrast to the results of Bennett et al. (2004), D_{Li} and D_{Zr} do not show the expected effects of higher jadeite component (Figs. 8c and 8d). D_{Li} for MEDSIL5244 (0.16 ±0.04) and MEDSIL1035A (0.25 ± 0.06) are within errors of most previous cpx-melt studies [e.g., DiAb (0.12 ± 0.02) and DiAn (0.20 ± 0.03) in Brenan et al. 1998; and 4EHE (0.21 ± 0.04) in Hill et al. 2000], despite the prediction that higher jadeite component should result in lower D_{Li} (Bennett et al. 2004). A compensating increase in D_{Li} due to increased melt polymerization does not explain the observed D_{Li} because Li^+ has moderate field strength (Ryerson and Hess 1978) and should not be affected by melt structure. Likewise, D_{Zr} does not increase in these experiments relative to experiments with less jadeite-rich cpx (Figs. 8c and 8d). Therefore, the effects of jadeite component suggested by Bennett et al. (2004) are inconsistent with the results in our study.

Second, *higher* proportions of jadeite in the cpx in the studies of Klemme et al. (2002) and Pertermann and Hirschmann (2002) result in partition coefficients of REE that are much *lower* than

those Bennett et al. (2004), suggesting increased jadeite component does not necessarily result in higher D_{REE}. Of course, the cpx in these studies are quite different from those in Bennett et al. (2004). Indeed, it is difficult to identify clearly the relative controls in Bennett et al. (2004) because of the multiple changes in cpx components. For example, the cpx in NCMAS not only differ from the CMAS cpx in their jadeite component, but also in their CaTs (0.37 vs. 0.24), Ca-eskolaite (0.04 vs. 0.20), and diopside (0.56 vs. 0.41) components, making it difficult to attribute the higher D_{REE} for the NCMAS experiment relative to the CMAS experiment simply to higher jadeite component. In summary, it is not clear from the larger body of cpx partitioning studies that jadeite component is a major influence on D_{REE}; within our study, there are better arguments for melt structure controlling the REE partition coefficients.

Effect of wollastonite component in cpx

Although the partition coefficients of REE have been shown to correlate positively with wollastonite content in cpx (McKay et al. 1986), this suggestion is not supported by our observations. For instance, experiment MEDSIL5244 with a higher CaO content (~22.1 wt%) in the cpx has lower D_{REE} than experiments MEDSIL2601 and MEDSIL9273 (with CaO of 18.4 and 19.1 wt%, respectively). Although CaO content will be important when significant amounts of Mg enter the M2 site, variations at the level observed in these experiments appears to have no discernible effect on partitioning of large cations. Thus, three major crystal-compositional controls identified previously as affecting cpx-melt partitioning do not explain the increase in REE partition coefficients noted here; this leaves melt structure as a final factor controlling cpx-melt partitioning to assess.

The effect of melt structure

The partitioning of trace elements between two immiscible silicate liquids depends on the extent of polymerization and the average charge density of cations in each melt (Watson 1976; Ryerson and Hess 1978; Schmidt et al. 2004). How a specific cation partitions between granitic and ferrobasaltic melts largely reflects its Z^+/r_i (where Z^+ and r_i are the valence and radius of the cation, respectively; Ryerson and Hess 1978). Cations with low charge density (Rb, Cs) partition into the more polymerized, silica-rich melt whereas highly charged cations partition into the less polymerized basaltic melt with ${}^{basalt/granite}D_{REE}$ being as large as 16.8 (Ryerson and Hess 1978). Intermediate charge density (Sr, Ba, Eu^{2+}) cations correspondingly show only a slight dependence on the polymerization of melt (Ryerson and Hess 1978). Therefore, low Z^+/r_i cations are expected to have ${}^{cpx\text{-}silicic\ melt}D/{}^{cpx\text{-}basaltic\ melt}D < 1$ whereas higher Z/r cations such as REE should have ${}^{cpx\text{-}silicic\ melt}D/{}^{cpx\text{-}basaltic\ melt}D > 1$.

Our results for ${}^{cpx/melt}D$ of La, Sm, Yb, Sr, Zr, and Ti as a function of NBO/T indicate that most elements except Zr conform to this general expectation (Fig. 9). To eliminate the effect of crystal composition on the partition coefficients, only partitioning between diopsidic cpx and their coexisting melts are shown in Figure 9. As discussed already, the partition coefficients for more polymerized melts increase dramatically relative cpx-basaltic melt partitioning. Melt structure controls on Sr partitioning are also consistent with expectation from Ryerson and Hess (1978). For instance, ${}^{cpx/melt}D_{Sr}$ (0.23–0.39) increases by factors from 2 to 5 relative to an average ${}^{cpx/melt}D_{Sr}$ value of 0.10 for cpx-basaltic melt (Skulski et al. 1994; Lundstrom et al. 1994, 1998; Hill et al. 2000), consistent with the predictions (Ryerson and Hess 1978). Notably, our result is also in good agreement with the D_{Sr} inferred from silica-rich glass-diopside pairs in mantle xenoliths (Vannucci et al. 1998).

However, in contrast with prediction of Ryerson and Hess (1976), D_{Zr} does not dramatically increase with NBO/T (Fig. 9e). *D*espite the high degree of melt polymerization, ${}^{cpx/melt}D_{Zr}$ in this study (0.14–0.23) is slightly lower than previous cpx-basaltic melt partitioning studies (e.g., 0.27 in Blundy et al. 1998; 0.28 in Hill et al. 2000; and 0.27 in Watson and Ryerson 1986). Notably, ${}^{cpx/melt}D_{Zr}$ agrees well with observed mineral-matrix partitioning between cpx and silica-rich glasses (Sisson 1991; Vannucci et al. 1998). The relatively constant D_{Zr} for vastly different silicate melts might be explained by the complex behavior of Zr incorporation into silica-rich melts. Ryerson (1985) suggests that Zr^{4+} may behave as both a network modifier in depolymerized melt and a network forming cation in polymerized melts. Lower NBO/T does not change the incompatible character of Zr in cpx, suggesting that the mineral-melt partitioning of Zr shows no dependence on non-bridging O atoms. Consistent with this, a recent study by Prowatke and Klemme (2005) indicates that partitioning of Zr between titanite and silicate melt does not significantly depend on melt composition either.

Although similar to Zr in Z^+/r_i, Ti does increasingly partition into cpx with decreasing NBO/T (Fig. 9f). For instance, the value of ${}^{cpx/melt}D_{Ti}$ in this study is as high as 1.04 (HISIL7262) and two samples from Draper and Green (1999) have even higher D_{Ti} (2.09 and 1.53, respectively). Similarly, the inferred D_{Ti} from Vannucci et al. (1998) also agrees well with this result. Thus, despite somewhat similar chemical behavior, Zr and Ti are affected distinctly by melt structure, with Ti behaving in accord with prediction of Ryerson and Hess (1978).

The REE partition coefficients in our study are dramatically higher than most previous cpx-melt partitioning studies (Figs. 8a–8c) and are consistent with a recent study of Gaetani (2004) that argued that melt structure becomes dominantly important below a threshold NBO/T value of 0.49. Unfortunately, no data exist for experiments having diopsidic cpx and NBO/T > 0.2 and < 0.4.

For a highly polymerized silicate melt with NBO/T < 0.4, small changes in melt structure have a dramatic effect. For instance, as the NBO/T shifts from 0.12 (MEDSIL2601 and MEDSIL9273) to 0.17 (MEDSIL5244), ${}^{cpx/melt}D_0$ for the REE changes from 3.62 to 1.23. Similarly, as NBO/T shifts from 0.08 to 0.10, ${}^{cpx/melt}D_0$ decreases from 1.95 (HISIL9163) to 1.09 (HISIL7262). Although NBO/T provides a consistent sense of a melt structure effect for a given composition, it does not allow an adequate description of the melt structure changes when both MEDSIL and HISIL compositions, with differing silica contents, are considered together. For instance, the higher silica content melts (e.g., HISIL7262) produce lower partition coefficients than the intermediate silica content melts (e.g., MEDSIL9273), opposite to what might be expected based on the simplest view of silica polymerization.

Although NBO/T has been used to describe the extent of melt

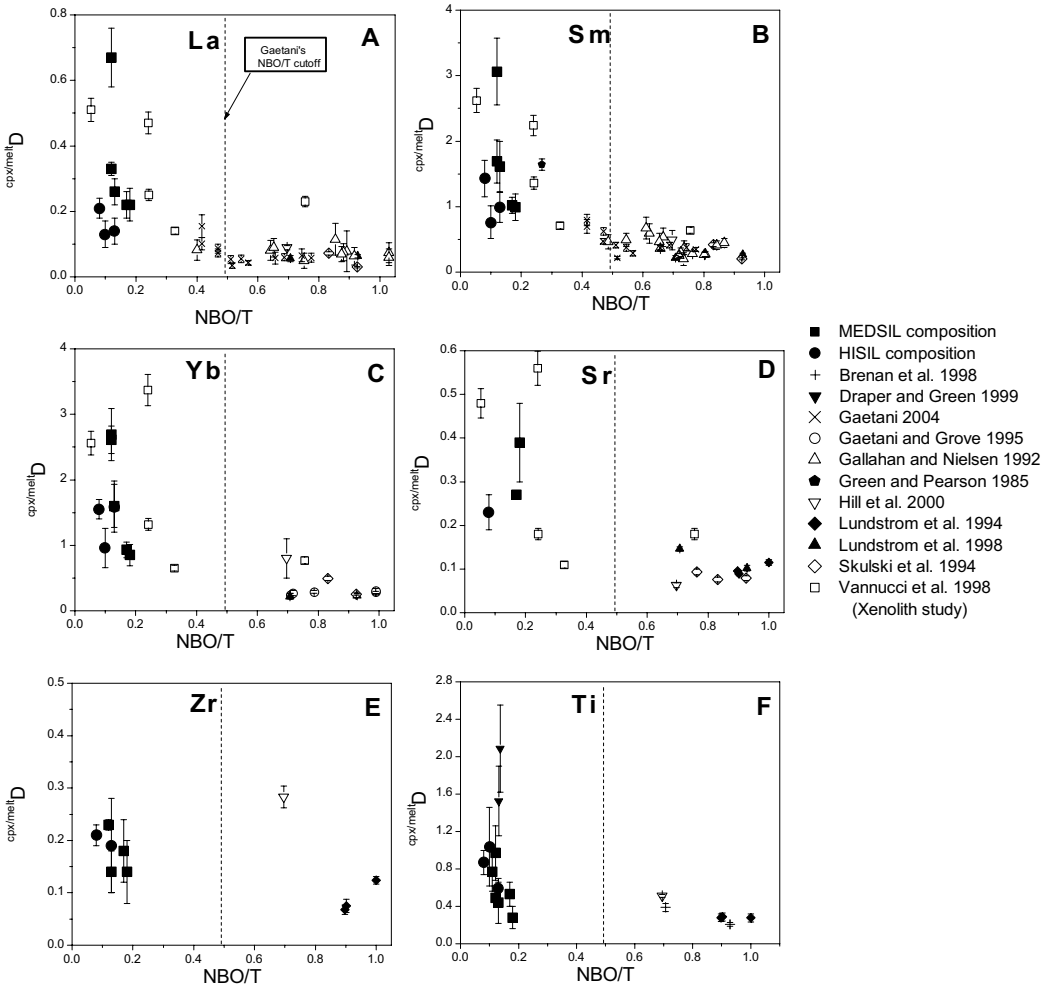

FIGURE 9. $^{cpx/melt}D$ for La, Sm, Yb, Sr, Zr, and Ti as a function of NBO/T of the glass (Mysen 1985). Dash line indicates the value of NBO/T (0.49) suggested by Gaetani (2004) at which the melt structure can have a significant influence on partition coefficients. Our REE partition coefficients agree with this interpretation showing dramatic increases at low NBO/T. Partition coefficients for Zr show no simple relationship with NBO/T whereas Ti increases at low NBO/T. Sources of data include Green and Pearson (1985), Gallahan and Nielsen (1992), Skulski et al. (1994), Gaetani and Grove (1995), Lundstrom et al. (1994, 1998), Brenan et al. (1998), Vannucci et al. (1998), Draper and Green (1999), Hill et al. (2000), and Gaetani (2004). Error bar of NBO/T is smaller than the symbol. The $^{cpx/melt}D$ data used here are selected based on the compositions of clinopyroxenes, which are diopsidic with $^{IV}Al < 0.16$ except for data from Gaetani (2004) and Vannucci et al. (1998). Al_2O_3 contents of the clinopyroxenes in Gaetani (2004) are 9.95–12.6 wt%. Data in Vannucci et al. (1998) are trace-element ratios between diopsidic clinopyroxene and silicic glasses from La Palma xenoliths.

polymerization for 20 years (Mysen and Virgo 1980), NBO/T may not provide a comprehensive description of melt structure at the level relevant to affecting element partitioning (Bennett et al. 2004). NBO/T, calculated by the method of Mysen et al. (1985) assumes that Si^{4+} and Ti^{4+} are network-forming cations in tetrahedral coordination. Because there are enough M^{2+} (Fe^{2+}, Ca^{2+}, and Mg^{2+}) and M^{+} (Na^{+} and K^{+}) cations to form Al^{3+} complexes for charge balance (Mysen et al. 1985), Al^{3+} is also a network-forming cation in tetrahedral coordination. Thus, NBO/T effectively treats M^{1+} and M^{2+} cations the same, and therefore does not account for the fundamentally different behaviors that these ions have in affecting melt properties. Indeed, Toplis and *D*ingwell (2004) have recently proposed that the effective NBO/T is higher than the calculated value with the offset between effective and calculated values being a function of the amounts of monovalent and divalent cations as calculated NBO values approach zero (e.g., as in this study).

The utility of our experiments is that they compare partitioning between melts of subtle compositional change and cpx of essentially identical composition. Within a single starting material (HISIL or MEDSIL), compositional changes in the melt mostly reflect variation in the CaO content whereas the compositional changes among starting materials reflect their total alkali and silica contents. The final melt composition of an experiment, especially for CaO and MgO contents, depends on the proportion of crystals. The effects of these changes on $^{cpx/melt}D_0$ (REE)

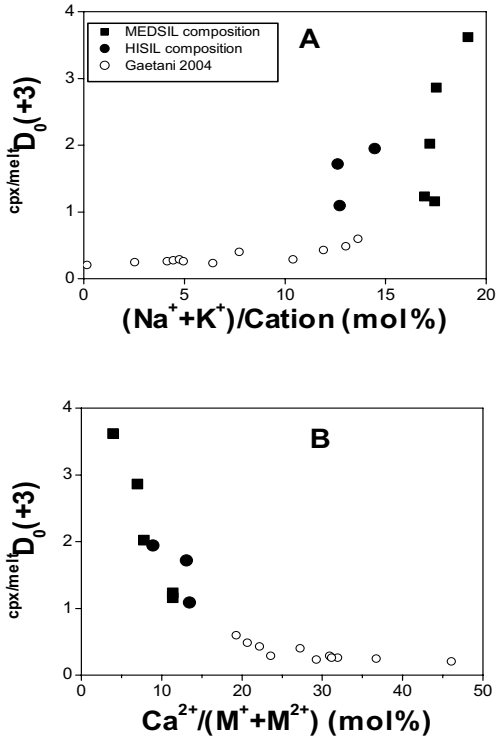

FIGURE 10. D_0 of REE as a function of molar ratio of $(Na^+ + K^+)$/cation (including quadri-, tri-, di-, and monovalent cations in melt) and $Ca^{2+}/(M^+ + M^{2+})$ in the melt. D_0 is correlated very well with $(Na^+ + K^+)$/cation only if MEDSIL or HISIL composition is considered separately in **a**. However, negative correlation of D_0 with $Ca^{2+}/(M^+ + M^{2+})$ shows good connection of two compositions in this study and the corrected data from Gaetani (2004) in **b**. Because the higher ^{IV}Al in cpx from Gaetani (2004) enhance the D_0 significantly, we have corrected these D_0 to the average ^{IV}Al (0.05) in this study using a regression based on the data shown in Figure 1b of Hill et al. (2000). The regression reflects a linear fit to the data shown in Hill et al. (2000) except data listed as Blundy unpublished, yielding $\log D_{REE} = 2.50^{IV}Al - 1.48$ with $R^2 = 0.72$.

are shown individually and in combination with the data of Gaetani (2004) (Fig. 10). Figure 10a shows that $^{cpx/melt}D_0$ (REE) correlates with the mol% total alkalis (of the total cations in the melt) for each composition, but that the MEDSIL or HISIL samples form separate trends offset from one another. In contrast, samples from the two compositions and Gaetani (2004) produce an excellent single correlation as a function of the ratio of molar $Ca^{2+}/(M^+ + M^{2+})$ of the melt (Fig. 10b), indicating that melt Ca content appears to be a dominant factor in element partitioning with these melts.

The roles of alkalis and Ca^{2+} in affecting melt structure have been investigated several ways, mostly through spectroscopic techniques (e.g., Cormier and Neuville 2004; Mysen 2004; Mysen and *D*ubinsky 2004; Neuville et al. 2004a, 2004b). An important finding has been that the reaction between Q^n structure units, $2Q^n = Q^{n-1} + Q^{n+1}$ shifts to the right as the Z^+/r_i of the modifying cations increase (Maekawa et al. 1991). (Q^n denotes species in silicate melt with different numbers of bridging oxygen, n.) Thus, as the Z^+/r_i increases with increasing CaO and decreasing Na_2O in the melt, the network becomes less regular with both larger and smaller sites in the structure produced. This increase in the number of large sites will be critically important to accommodating large REE ions at the hundreds of ppm level in these melts. Furthermore, because of the similarity of charge and size, REE are more likely to substitute for Ca^{2+} in the melt than Mg^{2+}, Fe^{2+}, or alkalis. Thus, larger $Ca^{2+}/(M^+ + M^{2+})$ results in more sites appropriate for REE^{3+} in the melt, reducing $^{cpx/melt}D_{REE}$. We emphasize that $Ca^{2+}/(M^+ + M^{2+})$ is probably only useful as a discriminator of melt structure in meta- or subaluminous melts where Al^{3+} is a network-former and charge balanced by M^+ and M^{2+}. Once the melt is Al-saturated and peraluminous, the behavior of Al^{3+} as a network-modifier also must be considered.

A thermodynamic explanation for the control of partition coefficients by melt Ca content follows from a simple expression of the likely species in the cpx and melt. Assuming REE are more likely to substitute for Ca^{2+} than other mono- or divalent cations (e.g., Na^+, Mg^{2+}) in the melt, a substitution mechanism is:

$$\left[(REE)_{2/3}MgSi_2O_6\right]_{cpx} + \left[Ca\text{-}NBO\right]_{melt} \leftrightarrow \left[CaMgSi_2O_6\right]_{cpx} + \left[(REE)_{2/3}\text{-}NBO\right]_{melt} \quad (2)$$

which, under equilibrium conditions, can be expressed as:

$$K = D_{REE} \times [Ca - NBO]/[CaMgSi_2O_6] \quad (3)$$

As shown above, the effect of the composition of cpx on $^{cpx/melt}D_{REE}$ is insignificant and can be assumed constant. Thus, as the activity of Ca^{2+} and $(Ca\text{-}NBO)_{melt}$ decrease, the partition coefficients must increase. Variations of the M^+ and M^{2+} contents of the melt could change the constitution of NBO-species and therefore partition coefficients of trace elements. However, as mentioned in Bennett et al. (2004), it might not change the NBO/T.

Application to hump-shaped REE patterns in mantle cpx crystals

These experiments were performed with the explicit purpose of constraining the partitioning and extraction of elements during melting of the shallow mantle, testing the hypothesis that the anomalous "humped" REE patterns observed in some abyssal peridotites reflect melting due to the diffusive infiltration of alkalis (Lundstrom 2000). Because the pressures are relatively low and the cpx compositions are relevant to depleted peridotite, these experiments are *not* intended to simulate early melting of fertile peridotite. Silicic melt coexisting with depleted peridotite is documented by interstitial xenolith glasses and may be evidenced in residual peridotites by high Na_2O contents of cpx crystals. Although the origin of these silicic melts remains debatable, our interpretation is that these melts reflect the effects of alkalis diffusing through interstitial melt in peridotite surrounding conduits for melt ascent (Lundstrom 2000, 2003). If this process significantly contributes to the total volume of melt derived from a given melting region, it would have important implications for how melting occurs and for the actual thermal regime relevant to mantle melting.

Our experimentally determined partition coefficients agree well with the partitioning inferred from concentrations of coexist-

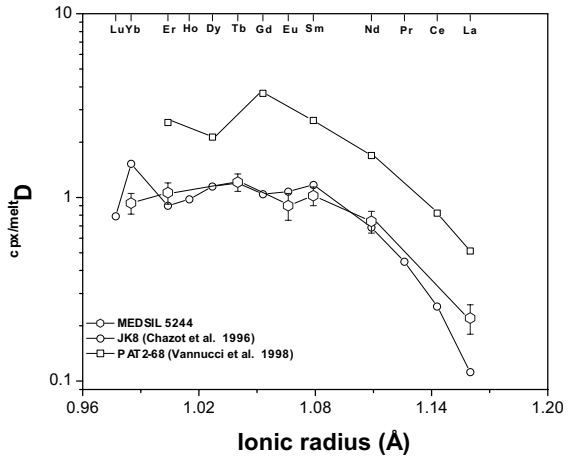

FIGURE 11. Ionic radius (Å) vs. $^{cpx/melt}D$ for REE in MEDSIL5244 along with observed diopside-xenolith glass pairs. The pattern of D_{REE} of MEDSIL5244 is consistent with inferred partitioning between clinopyroxene and coexisting glass in mantle xenoliths in the study of Chazot et al. (1996) (sample JK8) and Vannucci et al. (1998) (sample PAT2-68).

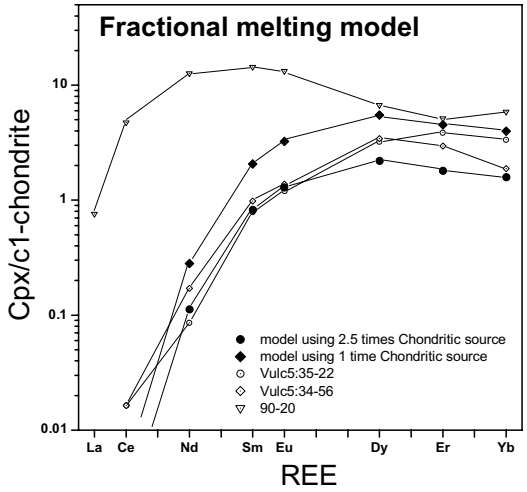

FIGURE 12. Chondrite-normalized REE concentrations of clinopyroxene after a two-step fractional-melting model. The details of the model are given in the text. Vulc5:35-22 and Vulc5:34-56 are from Johnson et al. (1990); 90-20 is from Hellebrand and Snow (2003). Using the partition coefficients of this study in a two-step fractional-melting model are able to reproduce the hump-shaped REE patterns peaking at Dy. However, these cannot explain patterns that peak at LREE such as those in 90-20 (Hellebrand et al). Although these patterns may be due to melt refertilization (Hellebrand and Snow 2003), increasing jadeite content of clinopyroxene (as observed in the 90-20) will continue to shift the peak in D_{REE} toward LREE, such that silicic melt-clinopyroxene partitioning may even explain these hump-shaped patterns.

ing diopside and silicic glass in harzburgite xenoliths from the Canary Islands (PAT2-68 in Vannucci et al. 1998) (Fig. 11). This consistency reinforces the assertion of Vannucci et al. (1998) that equilibrium between cpx and melts existed in the xenolith and suggests that our results may be applicable to melting processes occurring in the shallow mantle, particularly if silica-rich melts are involved in lithospheric melting (Wulff-Pedersen et al. 1996, 1999; Vannucci et al. 1998; Lundstrom et al. 2003). Inferred partitioning in another xenolith (JK8 from Chazot et al. 1996), determined by the ratio of REE concentrations between euhedral cpx and its surrounding melt pocket also agree with our results (Fig. 11). Notably, the cpx in JK8 also has high Na_2O (1.26 wt%), low Al_2O_3 content (4.42 wt%), and a hump-shaped REE pattern (Chazot et al. 1996). Similar hump-shaped REE patterns are also found in cpx with high Na_2O content in mantle harzburgites xenoliths from Huinan, NE China, which are suggested to result from melt-rock reaction involving olivine + orthopyroxene precipitation at the expense of cpx (Xu et al. 2003).

If diffusive fluxing of alkalis creates silicic, alkaline, and aluminous melts at shallow mantle depths beneath mid-ocean ridges (Lundstrom 2000), these partition coefficients may also be applicable to asthenospheric melting. Such a process may be evidence by the relatively high Na_2O concentrations in many cpx crystals of abyssal peridotites, which have otherwise been stripped of incompatible elements (e.g., Johnson et al. 1990). If so, the use of these partition coefficients could significantly change conclusions of abyssal peridotite partial melting models (e.g., Johnson et al. 1990; Hellebrand et al. 2002). For instance, hump-shaped REE patterns consistent with the maxima in $^{cpx/melt}D_{REE}$ occurring within the MREE have been observed repeatedly in some residual peridotite cpx (Johnson et al. 1990; Hellebrand et al. 2002; Hellebrand and Snow 2003) (Fig. 12). Johnson et al. (1990) suggested that these hump-shaped patterns could be explained by fractional melting in the garnet stability field followed by further melting in the spinel stability field. Similarly, Hellebrand et al. (2002), in a study of residual cpx in abyssal peridotites from the Central Indian Ridge, suggested that the hump-shaped patterns could be the product of <8% melting in the garnet stability field followed by ~13% critical (fractional) melting in the spinel stability field. In both of these models, garnet controls the bulk HREE budget and thus affects the MREE/HREE of the residual cpx, particularly after the garnet-

TABLE 6. Mineral-melt partition coefficients of REE and phase proportions used in the two-step fractional melting model

$^{Mineral/melt}D$*	Step 1				Step 2‡
	Olivine†	Opx†	Cpx†	Spinel†	Cpx
La	7×10^{-6}	0.0025	0.06	0.0006	0.22
Ce	1×10^{-5}	0.005	0.1	0.0006	0.36
Nd	7×10^{-5}	0.01	0.2	0.0006	0.77
Sm	0.001	0.02	0.3	0.001	1.21
Eu	0.001	0.02	0.37	0.001	1.12
Dy	0.004	0.05	0.44	0.002	1.36
Er	0.009	0.07	0.43	0.003	1.11
Yb	0.014	0.09	0.41	0.005	1.00

Phase§	Starting mode (vol%)	Melt mode (vol%)
Olivine	55	10
Opx	25	20
Cpx	18	68
Spinel	2	2

* From Table 7 of Hellebrand et al. (2002).
† Olivine, opx, and spinel use values that are 3 times those used in step 1.
‡ Using the partition coefficient data of MEDSIL5244 measured by SIMS except $^{cpx/melt}D_{Ce}$ and $^{cpx/melt}D_{Dy}$, which were calculated using the Lattice Strain model and parameters in Table 5.
§ The phase proportions from Table A2 of Johnson et al. (1990).

TABLE 7. Comparison of average composition of major elements of clinopyroxenes in Hellebrand and Snow (2003) with this study (all units in wt%)

	SiO_2	TiO_2	Al_2O_3	Cr_2O_3	FeO	MgO	MnO	CaO	NiO	Na_2O	K_2O	Total
HISIL*	53.61	0.32	4.63	1.24	3.17	18.44	–	17.48	–	1.07	0.03	100.00
MEDSIL†	54.37	0.30	3.56	0.02	2.61	17.90	–	19.80	–	1.10	0.08	99.82
N cpx‡	52.21	0.22	5.70	1.09	2.52	15.75	0.09	21.65	0.04	0.98	0.01	100.25
H cpx§	53.31	0.22	4.96	1.96	2.22	15.64	0.10	20.75	0.04	1.61	0.01	100.84

* Average cpx composition in all HISIL components.
† Average cpx composition in all MEDSIL components.
‡ Average composition of three cpx with normal REE pattern from Table 3 of Hellebrand and Snow (2003).
§ Average composition of three cpx with hump-shaped REE pattern from Table 3 of Hellebrand and Snow (2003).

spinel transition. This explanation does not make sense from the standpoint that early melting in the garnet stability field should enrich the HREE relative to MREE in the residual solid resulting in cpx in the spinel stability field also having HREE/MREE >1. Any melting in the spinel stability field using standard cpx-basalt partition coefficients should not result in residual cpx with HREE/MREE <1.

We developed a two-stage, non-modal fractional-melting model of REE concentration in residual abyssal peridotite cpx to examine the effect of the higher $^{cpx/melt}D_{MREE}$ found here, using the equations of fractional melting from Johnson et al. (1990) (Fig. 12). In the first stage, fractional melting of a depleted spinel lherzolite (2.5 × or 1 × C1-chondrite) begins at 70 km depth and ends at 35 km depth, using the spinel lherzolite stability field partition coefficients given in Hellebrand et al. (2002). In the second stage, because mantle minerals are in equilibrium with the melt enriched in SiO_2, Al_2O_3, and alkalis, the model continues fractional melting using partition coefficients based on experiment MEDSIL5244 from a depth of 35 to 10 km (Table 6). The total degree of melting (*f*) is 0.2 and this changes linearly with depth. Thus, the $^{cpx/melt}D_{REE}$ we use for the upper 25 km of the melting column is about 3× higher than the values of $^{cpx/melt}D_{REE}$ for melting in spinel stability field used by Hellebrand et al. (2002). Because the increased effect of melt structure will not only affect the partitioning of trace elements between melt and cpx, but also orthopyroxene, olivne, and spinel, we assume that the partition coefficients for orthopyroxene, olivine, and spinel also increase by a factor of 3 relative to those used in Hellebrand et al. (2002). We calculated values for $^{cpx/melt}D$ of Ce and Dy using the lattice strain model. Partition coefficients and starting mineral and melt modes are given in Table 6. REE concentrations are normalized to C1-chondrites (Sun and Mc*D*onough 1989).

Results of this fractional-melting model show that REE concentrations in residual cpx produce a hump-shaped pattern with the peak located in the MREE (*D*y). This result is consistent with the REE pattern observed in sample Vulc5:34-56 (Johnson et al. 1990), which has a similar hump-shaped REE pattern with the peak at *D*y (Fig. 12). The observed REE concentration of Vulc5:34-56 lies between the results of the two fractional-melting models (1× and 2.5× chondritic source). However, this model does not explain any REE patterns that peak in the LREE.

To reinforce further the connection among our experiments, observed hump-shaped REE patterns, and cpx composition, we note from the study of Hellebrand et al. (2002) that the cpx having hump-shaped REE patterns have higher Na_2O and lower Al_2O_3 contents than the cpx having normal REE patterns. Normal type (N-type) and cpx have an average Na_2O content of 0.98 wt% while H-types average 1.61 wt% (Table 7). This relationship suggests that the high-Na_2O H-type cpx might reflect final equilibrium with a silica-rich melt possibly produced by diffusive fluxing of alkalis (Lundstrom 2000).

The shift in the location of the peak REE partition coefficient toward lighter REE is consistent with the change expected as cpx becomes more Na_2O rich. Because the size of the $^{VIII}Na^{+}$ and $^{VIII}Ca^{2+}$ cations is 1.18 and 1.12 Å, respectively (Shannon 1976), an increase in the Na_2O content of a cpx should enlarge the size of the M2 site (e.g., Bennett et al. 2004). If so, the site will become more accommodating to larger cations, shifting the peak to lighter REE. This effect can be seen by comparison of the +3 parabola position for our partition coefficients with the positions of parabolas from Blundy et al. (1998) and Lundstrom et al. (1998) (Fig. 6).

Thus, although our model does not predict humps peaking at Sm as observed in sample 90-20 (Hellebrand and Snow 2003) or Er as observed in sample Vulc5:35-22 (Johnson et al. 1990), these features might reflect equilibrium between a silica-rich melt and cpx with even higher Na_2O contents than our study. For instance, H-type cpx (sample 90-20) of Hellebrand and Snow (2003) have significantly higher Na_2O contents than the cpx from our experiments so that the peak in REE partitioning should be shifted toward the lighter REE. Although these details need to be explored further, fractional melting in the shallow mantle in the presence of silica-rich melts and high Na_2O cpx might explain even these dramatically different cpx REE patterns. Two implications of this suggestion are that garnet need not be invoked to explain these patterns (e.g., Johnson et al. 1990; Hellebrand et al. 2002), and that silica-rich melts may be present and extracted in the shallowest portions of some mid-ocean ridge melting columns.

ACKNOWLEDGMENTS

We thank G. Gaetani and J. Blundy for constructive reviews, T. Green and M. Toplis for comments on an earlier version of the manuscript, and associate editor M. Hirschmann for editorial handling. We are also grateful for M. Pertermann, J. Kirkpatrick, and J. Li for suggestions on the piston cylinder experiments and J. Lee for technical assistance with the ion probe, which is partly supported by *D*OE grant *D*EFG02-91-ER45439. This work was supported by NSF EAR 0000924.

REFERENCES CITED

Bennett, S.L., Blundy, J.D., and Elliott, T. (2004) The effect of sodium and titanium on crystal-melt partitioning of trace elements. Geochimica et Cosmochimica Acta, 68, 2335–2347.
Blundy, J. and Wood, B. (2003) Partitioning of trace elements between crystals and melts. Earth and Planetary Science Letters, 210, 383–397.
Blundy, J.D. and Wood, B.J. (1994) Prediction of crystal-melt partition coefficients from elastic moduli. Nature, 372, 452–453.
Blundy, J.D., Robinson, J.A.C., and Wood, B.J. (1998) Heavy REE are compatible in clinopyroxene on the spinel lherzolite solidus. Earth and Planetary Science Letters, 160, 493–504.
Brice, J.C. (1975) Some thermodynamic aspects of the growth of strained crystals. Journal of Crystal Growth, 28, 249–253.
Chazot, G., Menzies, M.A., and Harte, B. (1996) Determination of partition coef-

ficients between apatite, clinopyroxene, amphibole, and melt in natural spinel lherzolites from Yemen: implications for wet melting of the lithospheric mantle. Geochimica et Cosmochimica Acta, 60, 423–437.
Cormier, L. and Neuville, D.R. (2004) Ca and Na environments in Na_2O-CaO-Al_2O_3-SiO_2 glasses: influence of cation mixing and cation-network interactions. Chemical Geology, 213, 103–113.
Draper, D.S. and Green, T.H. (1997) *P-T* phase relations of silicic alkaline, aluminous mantle-xenolith glasses under anhydrous and C-O-H fluid saturated conditions. Journal of Petrology, 38, 1187–1224.
——— (1999) *P-T* phase relations of silicic, alkaline, aluminous liquids: new results and applications to mantle melting and metasomatism. Earth and Planetary Science Letters, 170, 255–268.
Gaetani, G.A. (2004) The influence of melt structure on trace-element partitioning near the peridotite solidus. Contributions to Mineralogy and Petrology, 147, 511–527.
Gaetani, G.A. and Grove, T.L. (1995) Partitioning of rare earth elements between clinopyroxene and silicate melt: crystal-chemical controls. Geochimica et Cosmochimica Acta, 59, 1951–1962.
Green, T.H. and Pearson, N.J. (1985) Rare earth element partitioning between clinopyroxene and silicate liquid at moderate to high pressure. Contributions to Mineralogy and Petrology, 91, 24–36.
Hack, P., Nielsen R.L., and Johnston, A.D. (1994) Experimental determined rare-earth element and Y partitioning behavior between clinopyroxene and basaltic liquids at pressures up to 20 kbar. Chemical Geology, 117, 89–105.
Hamester, M., Wiederin, D., Wills, J., Kerl. W., and Douthitt, C.B. (1999) Strategies for isotope ratio measurements with a double focusing sector field ICP-MS. Fresenius' Journal of Analytical Chemistry, 364, 495–497.
Hart, S.R. and Dunn, T. (1993) Experimental cpx/melt partitioning of 24 trace elements. Contributions to Mineralogy and Petrology, 113, 1–8.
Hellebrand, E. and Snow, J.E. (2003) Deep melting and sodic metasomatism underneath the highly oblique-spreading Lena Trough (Arctic Ocean). Earth and Planetary Science Letters, 216, 283–299.
Hellebrand, E., Snow, J.E., Hoppe, P., and Hofmann, A.W. (2002) Garnet-field melting and late-stage refertilization in "residual" abyssal peridotites from the central Indian ridge. Journal of Petrology, 43, 2305–2338.
Hill, E., Wood, B.J., and Blundy, J.D. (2000) The effect of Ca-Tschermaks component on trace-element partitioning between clinopyroxene and silicate melt. Lithos, 53, 203–215.
Johnson, K.T.M. (1998) Experimental determination of partition coefficients for rare earth and high-field-strength elements between clinopyroxene, garnet, and basaltic melt at high pressure. Contributions to Mineralogy and Petrology, 133, 60–68.
Johnson, K.T.M., Dick, H.J.B., and Shimizu, N. (1990) Melting in the oceanic upper mantle: an ion microprobe study of diopsides in abyssal peridotites. Journal of Geophysical Research, 95, 2661–2678.
Klemme, S., Blundy, J.D., and Wood, B. (2002) Experimental constraints on major and trace-element partitioning during partial melting of eclogite. Geochimica et Cosmochimica Acta, 66, 3109–3123.
Lundstrom, C.C. (2000) Rapid diffusive infiltration of sodium into partially molten peridotite. Nature, 403, 527–530.
Lundstrom, C.C., Shaw, H.F., Ryerson, F.J., Phinney, D.L., Gill, J.B., and Williams, Q. (1994) Compositional controls on the partitioning of U, Th, Ba, Pb, Sr, and Zr between clinopyroxene and haplobasaltic melts: Implications for uranium series disequilibria in basalts. Earth and Planetary Science Letters, 128, 407–423.
Lundstrom, C.C., Shaw, H.F., Ryerson, F.J., and Gill, J., Williams, Q. (1998) Crystal chemical control of clinopyroxene-melt partitioning in the Di-Ab-An system: implications for elemental fractionations in the depleted mantle. Geochimica et Cosmochimica Acta, 62, 2849–2862.
Lundstrom, C.C., Hoernle, K., and Gill, J. (2003) U-series disequilibria in volcanic rocks from the Canary Islands: plume vs. lithospheric melting. Geochimica et Cosmochimica Acta, 67, 4153–4177.
Maekawa, H., Maekawa, T., Kawamura, K., and Yokokama, T. (1991) ^{29}Si MAS NMR investigation of the Na_2O-Al_2O_3-SiO_2 glasses. Journal of Physics and Chemistry, 95, 6822–6827.
McKay, G.A. (1986) Crystal/liquid partitioning of REE in basaltic systems: Extreme fractionation of REE in olivine. Geochimica et Cosmochimica Acta, 50, 69–79.
McKay, G., Wagstaff, J., and Yang, S.-R. (1986) Clinopyroxene REE distribution coefficients for Shergottites: the REE content of the Shergotty melt. Geochimica et Cosmochimica Acta, 50, 927–937.
McKenzie, D.P. and O'Nions, R.K. (1991) Partial melt distributions from inversion of rare earth element concentration. Journal of Petrology, 32, 1021–1091.
Mysen, B.O. (2004) Element partitioning between minerals and melt, melt composition, and melt structure. Chemical Geology, 213, 1–16.
Mysen, B.O. and Dubinsky, E.V. (2004) Melt structural control on olivine/melt element partitioning of Ca and Mn. Geochimica et Cosmochimica Acta, 68, 1617–1633.
Mysen, B.O. and Virgo, D. (1980) Trace-element partitioning and melt structure: an experimental study at 1 atm pressure. Geochimica et Cosmochimica Acta, 44, 1917–1930.
Mysen, B.O., Virgo, D., and Seifert, F.A. (1985) Relationships between properties and structure of aluminosilicate melts. American Mineralogist, 70, 88–105.
Neuville, D.R., Cormier, L., Flank, A.-M., Briois, V.R., and Massiot, D. (2004a) Al speciation and Ca environment in calcium aluminosilicate glasses and crystals by Al and Ca K-edge X-ray absorption spectroscopy. Chemical Geology, 213, 153–163.
Neuville, D.R., Cormier, L., and Massiot, D. (2004b) Al environment in tectosilicate and peraluminous glasses: A ^{27}Al MQ-MAS NMR, Raman, and XANES investigation. Geochimica et Cosmochimica Acta, 68, 5071–5079.
Pertermann, M. and Hirschmann, M.M. (2002) Trace-element partitioning between vacancy-rich eclogitic clinopyroxene and silicate melt. American Mineralogist, 87, 1365–1376.
Pertemann, M. and Lundstrom, C. (2006) Phase equilibrium experiments at 0.5 GPa and 1100–1300 °C on a basaltic andesite from Arenal volcano, Costa Rica. Journal of Volcanology and Geothermal Research, accepted.
Prowatke, S. and Klemme, S. (2005) Effect of melt composition on the partitioning of trace elements between titanite and silicate melt. Geochimica et Cosmochimica Acta, 69, 695–709.
Ray, G.L., Shimizu, N., and Hart, S.R. (1983) An ion microprobe study of the partitioning of trace elements between clinopyroxene and liquid in the system diopside-albite-anorthite. Geochimica et Cosmochimica Acta, 47, 2131–2140.
Ryerson, F.J. (1985) Oxide solution mechanisms in silicate melts: systematic variations in the activity coefficient of SiO_2. Geochimica et Cosmochimica Acta, 49, 637–649.
Ryerson, F.J. and Hess, P.C. (1978) Implications of liquid-liquid distribution coefficients to mineral-liquid partitioning. Geochimica et Cosmochimica Acta, 42, 921–932.
Salters, V.J.M. and Longhi, J. (1999) Trace-element partitioning during the initial stages of melting beneath mid-ocean ridges. Earth and Planetary Science Letters, 166, 15–30.
Schmidt, M.W., Bogaerts, M., Pertermann, M., and Günther, D. (2004) Trace-element partitioning between coexisting silicate melts: the effect of melt composition. Transactions of the American Geophysical Union, 85, V11C-06.
Shannon, R.D. (1976) Revised effective ionic radii and systematic studies of interatomic distances in halides and chalcogenides. Acta Crystallographica, A32, 751–767.
Sisson, T.W. (1991) Pyroxene-high silica rhyolite trace-element partition coefficients measured by ion microprobe. Geochimica et Cosmochimica Acta, 55, 1575–1585.
Skulski, T., Minarik, W., and Watson, E.B. (1994) High-pressure experimental trace-element partitioning between clinopyroxene and basaltic melts. Chemical Geology, 117, 127–147.
Sun, S.-S. and McDonough, W.F. (1989) Chemical and isotopic systematics of oceanic basalts: implications for mantle composition and processes. In A.D. Saunders and M.J. Norry, Eds., Magmatism in the Ocean Basins, 42, p. 313–345. Geological Society of London Special Publication, Blackwell Scientific Publications, Oxford.
Ulmer, P. and Luth, R.W. (1991) The graphite-COH fluid equilibrium in P, T, f_{O2} space; an experimental determination to 30 kbar and 1600 °C. Contributions to Mineralogy and Petrology, 106, 265–272.
Vannucci, R., Bottazzi, P., Wulff-Pedersen, E., and Neumann, E.-R. (1998) Partitioning of REE, Y, Sr, Zr, and Ti between clinopyroxene and silicate melts in the mantle under La Palma (Canary Islands): implications for the nature of the metasomatic agents. Earth and Planetary Science Letters, 158, 39–51.
Watson, E. (1976) Two-liquid partition coefficients: experimental data and geochemical implications. Contributions to Mineralogy and Petrology, 56, 119–134.
Watson, E.B. (1985) Henry's law behavior in simple systems and magmas: criteria for discerning concentration-dependent partition coefficients in nature. Geochimica et Cosmochimica Acta, 49, 917–923.
Watson, E.B. and Ryerson, F.J. (1986) Partitioning of zirconium between clinopyroxene and magmatic liquids of intermediate composition. Geochimica et Cosmochimica Acta, 50, 2523–2526.
Wood, B.J. and Blundy, J.D. (1997) A predictive model for rare earth element partitioning between clinopyroxene and anhydrous silicate melt. Contributions to Mineralogy and Petrology, 129, 166–181.
Wulff-Pedersen, E., Neumann, E.-R., and Jensen, B.B. (1996) The upper mantle under La Palma, Canary Islands: formation of Si-K-Na-rich melt and its importance as metasomatic agent. Contributions to Mineralogy and Petrology, 125, 113–139.
Wulff-Pedersen, E., Neumann, E.-R., Vannucci, R., Bottazzi, P., and Ottolini, L. (1999) Silicic melts produced by reaction between peridotite and infiltrating basaltic melts: ion probe data on glasses and minerals in veined xenoliths from La Palma, Canary Island. Contributions to Mineralogy and Petrology, 137, 59–82.
Xu, Y.-G., Menzies, M.A., Thirlwall, M., Huang, X., and Chen, X. (2003) "Reactive" harzburgites from Huinan, NE China: products of the lithosphere-asthenosphere interaction during lithospheric thinning? Geochimica et Cosmochimica Acta, 67, 487–505.

MANUSCRIPT RECEIVED FEBRUARY 6, 2005
MANUSCRIPT ACCEPTED APRIL 10, 2006
MANUSCRIPT HANDLED BY MARC HIRSCHMANN